STUDYING THE WARM-HOT INTERGALACTIC MEDIUM IN EMISSION

Y. Takei[1], E. Ursino[2], E. Branchini[2], T. Ohashi[3], H. Kawahara[3], K. Mitsuda[1], L. Piro[4], A. Corsi[4], L. Amati[5],
J. W. den Herder[6], M. Galeazzi[7], J. Kaastra[6,8], L. Moscardini[9,10], F. Nicastro[11], F. Paerels[12],
M. Roncarelli[9], and M. Viel[13,14]

[1] Institute of Space and Astronautical Science, Japan Aerospace Exploration Agency, 3-1-1 Yoshinodai, Chuo-ku, Sagamihara,
Kanagawa 252-5210, Japan; takei@astro.isas.jaxa.jp
[2] Dipartimento di Fisica, Università degli Studi "Roma Tre" via della Vasca Navale 84, I-00146 Roma, Italy
[3] Department of Physics, School of Science, Tokyo Metropolitan University, 1-1 Minami-Osawa, Hachioji, Tokyo 192-0397, Japan
[4] INAF-Istituto di Astrofisica Spaziale Fisica Cosmica, Via del Fosso del Cavaliere 100, I-00133 Roma, Italy
[5] INAF-Istituto di Astrofisica Spaziale e Fisica Cosmica Bologna, via P. Gobetti 101, I-40129 Bologna, Italy
[6] SRON Netherlands Institute for Space Research, Sorbonnelaan 2, 3584 CA Utrecht, The Netherlands
[7] Physics Department of University of Miami, 319 Knight Physics Building, Coral Gables, FL 33164, USA
[8] Astronomical Institute, University of Utrecht, Postbus 8000, 3508, TA Utrecht, The Netherlands
[9] Dipartimento di Astronomia, Università di Bologna, via Ranzani 1, I-40127 Bologna, Italy
[10] INFN/National Institute for Nuclear Physics, Sezione di Bologna, Via Berti Pichat 6/2, I-40127 Bologna, Italy
[11] INAF-Osservatorio Astronomico di Roma,via Frascati 33, I00040 Monteporzio-Catone (RM), Italy
[12] Columbia Astrophysics Laboratory and Department of Astronomy, Columbia University, 550 West 120th Street, New York, NY 10027, USA
[13] INAF-Osservatorio Astronomico di Trieste, via Tiepolo 11, I-34131 Trieste, Italy
[14] INFN/National Institute for Nuclear Physics, Via Valerio 2, I-34127 Trieste, Italy

ABSTRACT

We assess the possibility of detecting the warm-hot intergalactic medium in emission and characterizing its physical conditions and spatial distribution through spatially resolved X-ray spectroscopy, in the framework of the recently proposed *DIOS*, *EDGE*, *Xenia*, and *ORIGIN* missions, all of which are equipped with microcalorimeter-based detectors. For this purpose, we analyze a large set of mock emission spectra, extracted from a cosmological hydrodynamical simulation. These mock X-ray spectra are searched for emission features showing both the O VII Kα triplet and O VIII Lyα line, which constitute a typical signature of the warm-hot gas. Our analysis shows that 1 Ms long exposures and energy resolution of 2.5 eV will allow us to detect about 400 such features per deg^2 with a significance $\geqslant 5\sigma$ and reveals that these emission systems are typically associated with density $\sim$100 above the mean. The temperature can be estimated from the line ratio with a precision of $\sim$20%. The combined effect of contamination from other lines, variation in the level of the continuum, and degradation of the energy resolution reduces these estimates. Yet, with an energy resolution of 7 eV and all these effects taken into account, one still expects about 160 detections per deg^2. These line systems are sufficient for tracing the spatial distribution of the line-emitting gas, which constitute an additional information, independent from line statistics, to constrain the poorly known cosmic chemical enrichment history and the stellar feedback processes.

Key words: cosmology: observations – intergalactic medium – large-scale structure of universe – X-rays: diffuse background

Online-only material: color figures

1. INTRODUCTION

After more than 10 years, the so-called missing baryon problem is far from being solved. The original claim of Fukugita et al. (1998) that the observational census of cosmic baryons in the local universe falls short of the expected cosmological mean (Burles & Tytler 1997; Barlow & Tytler 1998; Spergel et al. 2003; Komatsu et al. 2009) has gained even more statistical significance (Fukugita & Peebles 2004; Danforth & Shull 2005) and it is now generally accepted that a large fraction of the baryons ($\sim$40%) is not accounted for by observations at $z \sim 0$. This fact is even more surprising if one considers the fact that the baryon density in the Lyα forest at redshift $z = 2$–3 (Weinberg et al. 1997; Rauch 1998) accounts for about all expected baryons whereas the nucleons in the Lyα forest at $z \sim 0$ contributes to less than 30% of the cosmic mean (Bregman 2007).

Although baryons provide a small contribution to the cosmological mass-energy density, they are key players in forming stars and galaxies and determining the cosmochemical evolu-tion of the diffuse gas. In addition, being the only component that interacts with the electromagnetic radiation, they are the sole probe for investigating the physics of the formation and evolution of visible cosmic structures and infer the co-evolution of the underlying dark matter distribution.

Cosmological numerical simulations have provided a solution to this apparent paradox suggesting that missing baryons at $z < 1$ are distributed in a network of filaments with temperature 10^5–10^7 K with density significantly above the cosmic mean but below that typically found in virialized structures like galaxy clusters. This phase is called warm-hot intergalactic medium (WHIM). These results, which constitute one of the rare examples in cosmology in which theory leads observations, explain why these baryons have escaped observations so far and indicate the best strategy to detect them. Indeed, the WHIM is expected to be so highly ionized that it can only be seen in the UV and X-ray bands but the signal should be very weak because of its relatively low density. Therefore, it is not surprising that current observations in the UV and X-ray bands provide weak constraints to the WHIM models.

In the UV band, O VI absorption lines ($\lambda = 1032, 1038$ Å) have been detected along the lines of sight to $\sim$50 active galactic nuclei (AGNs; e.g., Danforth & Shull 2005, 2008; Tripp et al. 2008). Their cumulative number per unit redshift as a function of the line equivalent width (hereafter the dN/dz statistics) is consistent with the predictions of numerical models (see, e.g., Cen & Fang 2006; Branchini et al. 2009). However, it is debated how reliably the observed O VI absorption lines trace the WHIM since their width seems too small to be produced by warm-hot material. This means that either the observed lines trace the local Lyα forest rather than the WHIM or that the gas is two phased: a photoionized gas responsible for the Lyα absorption and shock-heated WHIM responsible for the O VI lines. Recent numerical simulations carried out to investigate the physical properties of the intergalactic medium (IGM) have helped to clarify the issue (Wiersma et al. 2009; Oppenheimer & Davé 2009; Smith et al. 2011; Tepper-García et al. 2011). These simulations have shown that the thermal state of the IGM at $z \sim 0$ is significantly affected by a number of physical processes like galactic wind, AGN feedback, metal line cooling, photoionization by background radiation, and sub-resolution turbulence. Although it is non-trivial to compare the results of different works and not all these works seem to converge to the same results, it is remarkable that two of them (Smith et al. 2011; Tepper-García et al. 2011) indicate that about a third of the O VI absorbers are photoionized and trace the Lyα forest at $z \sim 0$ while the rest of them trace the WHIM. An upper limit can nevertheless been worked out: if all gas is multi-phased, i.e., in the limit in which all the observed O VI lines are produced by the WHIM, then the O VI can probe no more than 7%–10% of the baryons (Danforth & Shull 2005; Tripp et al. 2006; Danforth 2009). With the inclusion of the thermally broadened Lyα absorbers (BLAs) recently observed by Danforth et al. (2010) and Narayanan et al. (2010a, 2010b), these estimates are boosted up by a factor of $\sim$2, i.e., UV observations are capable of probing $\sim$20% of the baryons in the local universe (Danforth et al. 2010). Nevertheless, whereas O VI might be a useful signpost for a non-negligible fraction of the missing baryons, the bulk of the WHIM cannot be investigated through UV spectroscopy. X-ray band observations are required.

In the soft X-ray band, the residual unresolved background after point-source subtraction possibly constitutes the second observational evidence of the WHIM. So far the tightest constraints have been obtained by Hickox & Markevitch (2007a, 2007b) after removing all contributions associated with X-ray, optical, and IR sources in the Chandra Deep Fields. Their analysis has shown that the residual background in the 0.65–1 keV energy band cannot be accounted for by AGN below the resolution limit. Instead, it appears to be consistent with the expected integrated emission contributed by the WHIM, as predicted by models based on hydrodynamical simulations (e.g., Roncarelli et al. 2006). The intensity of the diffuse X-ray background constitutes a weak constraint on the WHIM properties. Additional constraints can be obtained by identifying the WHIM signature in the angular correlation properties of the X-ray background, like in the recent analysis of Galeazzi et al. (2009).

Hydrodynamical simulations show that the best way to investigate the WHIM is by observing the X-ray emission or absorption lines of highly ionized element like C, N, O, Ne, Mg, and Fe. Deep X-ray spectroscopy has indeed been performed to detect such lines. From a theoretical viewpoint, the possibility of detecting and studying the WHIM in the absorption spectra of X-ray-bright objects like AGNs or gamma-ray bursts has been thoroughly discussed both from a general perspective (e.g., Kravtsov et al. 2002; Klypin et al. 2003; Chen et al. 2003; Viel et al. 2005; Cen & Fang 2006) and by considering observations carried out with some specific instrument (Viel et al. 2003; Yoshikawa et al. 2003, 2004; Kawahara et al. 2006; Paerels et al. 2008; Branchini et al. 2009). From the observational side, the analysis of the absorption spectra has lead to several claimed WHIM detections (e.g., Fang et al. 2002; Mathur et al. 2003; Nicastro et al. 2005) whose statistical significance has been questioned by subsequent studies (Rasmussen et al. 2007; Kaastra et al. 2006), reflecting the fact that these measurements are at the limits of current instrumental capabilities. The attempts to detect absorption lines associated with dense parts of large-scale structure lead to marginal detections with less than 4σ significance (Fujimoto et al. 2004; Takei et al. 2007; Buote et al. 2009; Fang et al. 2010; Zappacosta et al. 2010).

Studying the WHIM in absorption offers advantages and disadvantages. The advantage is that line detection depends on the source flux with no need to worry about foreground contributions. In addition, the line strength depends on the density of the intervening absorber, allowing one to probe regions of moderate overdensity. The obvious drawback is that one can only probe the WHIM along the few lines of sight to X-ray-bright objects, making it very difficult to trace its spatial distribution (but see Viel et al. 2003 for a possible way of probing the WHIM clustering in absorption).

On the other hand, studying the WHIM in emission is considerably harder but potentially more rewarding. The main difficulty is represented by the fact that line detection depends now on the capability of modeling the various contributions to the soft X-ray foreground, which, unfortunately, are poorly constrained by observational data (McCammon et al. 2002; Smith et al. 2005, 2007; Henley et al. 2007; Henley & Shelton 2008; Gupta et al. 2009; Yoshino et al. 2009). It is therefore not surprising if only a few WHIM detections have been claimed in continuum emission (Zappacosta et al. 2005; Mannucci et al. 2007; Takei et al. 2007; Werner et al. 2008). The main reward constitutes the possibility of tracing the three-dimensional distribution of the WHIM (Cen & Fang 2006) and quantifying its spatial and angular correlation properties (Ursino & Galeazzi 2006; Ursino et al. 2010). In addition, since X-ray emissivity scales with the square of the gas density, we expect the emission signal to be dominated by high-density regions, effectively complementing the absorption studies.

In this work, we will investigate the possibility of detecting, studying, and characterizing the WHIM in emission. In order to observe the weak WHIM emission features, a detector with a large grasp (effective area $\times$ field of view (FOV)) is mandatory. In addition, to separate the WHIM lines from other spectral features contributed by other sources a good energy resolution is also required. A number of recently proposed X-ray satellite missions such as *DIOS* (Ohashi et al. 2010), *EDGE* (Piro et al. 2009), *Xenia* (Burrows et al. 2010), and *ORIGIN* (den Herder et al. 2011) meet these requirements. We will assume observations with the detectors on board the proposed *EDGE* and *Xenia* missions. The detailed characteristics of these two X-ray satellites are presented in Piro et al. (2009)[15] and Burrows et al. (2010). For our purposes, the most relevant instrument is the cryogenic microcalorimeter-based spectrometer array: CRIS (Cryogenic Imaging Spectrometer). CRIS has the energy range of 0.2–2.2 keV (goal 0.1–3 keV), the energy

---

[15] Also see http://projects.iasf-roma.inaf.it/EDGE.

resolution of $\Delta E = 2.5$ eV (goal 1 eV) at 5.9 keV, the FOV of $0°.9 \times 0°.9$ (goal $1°.1 \times 1°.1$), the effective area $A = 1000$ cm^2 (goal 1300 cm^2) at 0.5 keV, and the angular resolution (half-power diameter) of $\Delta\theta = 4'$ (goal $2'.5$). The *DIOS* spectrometer has a similar energy resolution but a factor of 10 smaller grasp than *CRIS* on board *EDGE* or *Xenia*. *ORIGIN* is planned to have a better angular resolution $<30''$, at the expense of energy resolution ($\Delta E = 3$–5 eV). In this work we refer to the adopted baseline of the *EDGE* and *Xenia* spectrometer as a reference case and explore the effect of a different energy resolution, chosen in the range [1–7] eV. In contrast, we do not explore the angular resolution better than $1'.3$, because the typical angular size of the WHIM above detection threshold is $>2'$–$3'$.

The layout of this paper is as follows. In Section 2, we introduce the WHIM model used in this work from which we obtain the simulated surface brightness (SB) maps and emission spectra analyzed in this work. In Section 3, the problem of detecting the WHIM emission lines and computing their relevant statistics is addressed. In Section 4, we study the physical properties of the regions in which the WHIM can be detected in emission and assess the possibility of measuring the gas temperature from line ratios. In Section 5, we investigate the possibility of tracing the spatial distribution of the WHIM. In Section 6, we quantify the impact of energy resolution and line contamination from different sources. In Section 7, we address the question of to what extent we can discriminate among different models of stellar feedback and metal diffusion, using emission studies. Finally, we discuss the main results and conclude in Section 8.

2. MODELING THE WHIM

Hydrodynamical simulations provide the best way of studying the properties of the WHIM (see, e.g., Cen & Ostriker 1999a, 1999b; Davé et al. 2001; Chen et al. 2003; Borgani et al. 2004; Cen & Ostriker 2006; Oppenheimer & Davé 2008; Bertone et al. 2010; Tornatore et al. 2010). Their analysis has revealed that the missing baryon problem finds its natural solution in a standard ΛCDM framework in which the WHIM is heated up to temperatures of 10^5–10^7 K mostly by means of hydrodynamical shocks resulting from the buildup of cosmic structures at scales that are entering the nonlinear regime of density fluctuation growth. Additional heating/cooling mechanisms like stellar and AGN feedback, galactic superwinds, and radiative cooling, and ionization by background radiation further modify the thermal state of the gas. Despite the recent advances in modeling these mechanisms (Cen & Ostriker 2006; Cen & Fang 2006; Bertone et al. 2010; Tornatore et al. 2010; Shen et al. 2010; Wiersma et al. 2009; Oppenheimer & Davé 2009; Smith et al. 2011; Tepper-García et al. 2011), we still do not have a firm physical understanding of the effects of stellar feedback, chief among which is metal enrichment.

Indeed, metal enrichment is so important in determining the observational properties of the WHIM that, following Branchini et al. (2009), we prefer to specify gas metallicity after the simulation run (i.e., in the post-processing phase) rather than self-consistently during the numerical simulation. The resulting WHIM model has been shown to fulfill all existing observational constraints ranging from the dN/dz of the O VI and O VII absorption lines to the SB of the diffuse X-ray background. So, although effective, the WHIM model used in this work is not self-consistent. However, given the existing uncertainties in predicting metal abundances, in this work we will not rely on a single, sophisticated WHIM model.

Instead, in an attempt to account for theoretical uncertainties, we will consider two WHIM models that have been obtained from the same hydrodynamical simulations but by adopting different prescriptions for the gas metallicity.

Our WHIM models have been obtained from the hydrodynamical simulation of Borgani et al. (2004) performed with the GADGET-2 Lagrangian code (Springel 2005) in a computational box of size $192 \, h^{-1}$ comoving Mpc, loaded with 480^3 dark matter and 480^3 gas particles. Dark matter and gas particles have masses of $4.62 \times 10^9 \, h^{-1} \, M_\odot$ and $6.93 \times 10^8 \, h^{-1} \, M_\odot$, respectively. The Plummer-equivalent gravitational softening is $\epsilon = 7.5 \, h^{-1}$ kpc at $z = 0$, fixed in physical units between $z = 2$ and $z = 0$, i.e., the redshift interval relevant for the study of the WHIM. The background cosmological model is a flat ΛCDM with $\Omega_\Lambda = 0.7$, $\Omega_b = 0.04$, $H_0 = 70$ km s^{-1} Mpc^{-1} ($h = 0.7$), and power spectrum normalization $\sigma_8 = 0.8$. This numerical experiment uses simple recipes to account for the main non-gravitational heating and cooling mechanisms, namely: (1) the star formation process that is treated by adopting a sub-resolution multi-phase model for the interstellar medium (Springel & Hernquist 2003), (2) the feedback from SNe that includes the effect of weak galactic outflows, and (3) the radiative cooling assuming zero metallicity and heating/cooling from the photoionizing UV background by Haardt & Madau (1996). Finally, to construct our mock emission spectra we have considered all available simulation outputs out to $z = 0.5$.

As mentioned above, the gas metallicity has been specified in the post-processing phase and, to account for the scatter in model predictions, we have explored two different scenarios. In the first one, which we call model B1, we have adopted the deterministic metallicity–density relation $Z = \min(0.3, 0.005(1 + \delta_g)^{1/2})$, where δ_g is $\rho_{gas}/\langle\rho_{gas}\rangle - 1$, that Croft et al. (2001) have proposed to match the average relation measured in numerical experiments. This is a conservative model that typically underestimates the line emissivity since it ignores the large scatter in the Z–δ_g relation which would enhance the contribution of the line emission from regions characterized by moderate gas overdensity, like the WHIM. For this reason, the B1 model should be regarded as a generous lower bound to our detectability estimates. In the second model, dubbed B2, we do account for the large scatter in the metallicity–density relation. This scatter reflects the fact that the metal abundance at a given location is not simply determined by the underlying gas density but also by the thermal and chemical history of the gas particles. Since it would be hard to model this scatter analytically we resort to hydrodynamical simulations. For this reason, we have enforced the same Z–δ_g relation measured by Cen & Ostriker (1999a, 1999b) in their numerical experiment. In practice, we use the density–metallicity scatter plot measured at $z = 0$ in the Cen & Ostriker (1999b) simulation to derive a two-dimensional probability distribution which is then fed into a Monte Carlo procedure to assign metallicity to gas particles with known density in the Borgani et al. (2004) simulation. The result is a metallicity model with the same Z–δ_g relation plotted in Figure 2 of Cen & Ostriker (1999a) and characterized by a 1σ scatter of $\sim$0.3 dex. Note that we did not use the metallicity of the Borgani et al. (2004) simulation itself since the metal diffusion mechanism built in the SPH code reproduces the correct metal content in high-density regions, like the intracluster medium, but systematically underestimates the metal abundance in the typical WHIM environments.

We stress the fact that the metallicity assigned in the post-processing is not self-consistent with the thermal state of the gas

which, in the simulation considered in this work, is determined ignoring the role of metal cooling. In fact, recent numerical experiments show that the thermal state of the diffuse gas can be significantly altered by metal cooling (Wiersma et al. 2009; Oppenheimer & Davé 2009; Smith et al. 2011; Tepper-García et al. 2011). However, including the effect of metal cooling is beyond the scope of this paper. Instead, we attempt to bracket the uncertainties that derive from our simplification by adopting two very different density–metallicity relations, confident that the deterministic density–metallicity relation will provide very conservative predictions for the detectability of the WHIM.

To determine the ionization balance, we have assumed pure collisional ionization equilibrium (CIE) and not hybrid collisional and photoionization equilibrium as in Branchini et al. (2009). The use of the CIE assumption is justified by the fact that in this work we are interested in emission spectra whose intensity scales with the squared density of the gas and thus it is heavily weighted toward high-density peaks where the ionization is basically determined by collisions. Branchini et al. (2009) were interested in absorption lines which typically trace the WHIM in regions of moderate overdensity where photoionization cannot be neglected. For this reason, we have assumed CIE and used the APEC thermal model included in the code XSPEC (Smith et al. 2011) to compute emission spectra (Ursino & Galeazzi 2006). The resulting mock X-ray spectra contains all metal lines but here we focus on the strongest ones only: the O VIII Lyα line ($E = 0.653$ keV) and the O VII Kα triplet ($E = 0.561, 0.569$, and 0.574 keV).

Model B2 agrees with all available observational constraints and, from a theoretical viewpoint, predicts a phase-space diagram (shown in Figure 6 of Branchini et al. 2009) which is remarkably close to that of Cen & Ostriker (2006, shown in Figure 6 of their paper), a fact that further increases our confidence in model B2. Therefore, in this work we consider B2 as the reference model and regard predictions from model B1 as a generous lower bound.

One final caveat for model B2: this model is known to overestimate the X-ray emissivity in high-density ($\delta_g > 10^3$) environments, i.e., emission from gas in groups and clusters (Ursino et al. 2011). While the precise reason for this systematics is unknown, a plausible explanation is represented by the fact that in our model we have assumed primordial composition in the cooling function, instead of updating the cooling rate according to the evolving metallicity of the gas. The analysis of Bertone et al. (2010) suggests that this would artificially increase the emissivity in regions with high density. Brighter emission from group-like environments increases the chance superposition from strong emission lines, like those of the FeL complex, that may contaminate or even outshine the weaker O lines, artificially reducing our theoretical estimate of WHIM detection. We will quantify these effects in Section 6.1. We again stress the fact that the inclusion of metal line cooling may have an impact on both the line SB and the thermal state of the gas. We qualitatively discuss the expected impact of metal cooling in Section 8.
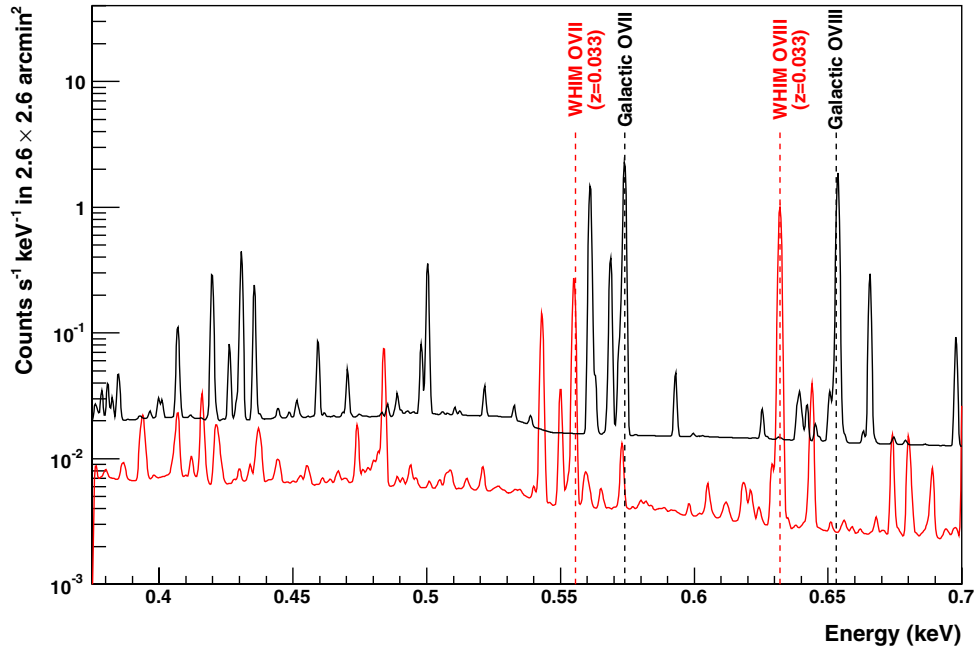
2.1. Mock Emission Spectra

The detailed procedure used to produce the mock spectra is described in detail in Ursino et al. (2010), here we provide a brief summary. To compute the mock X-ray spectra we have considered all gas particles within a light cone extracted from the hydrodynamical simulation, out to $z = 0.51$. The light cone is formed by stacking the simulation outputs corresponding to seven redshift intervals, each one of them corresponding to a comoving depth of 192 h^{-1} Mpc. We do not consider the WHIM at $z > 0.5$ since in that case the O VII lines would be redshifted to energies at which a number of emission lines due to L and M transitions of heavier metals make identification of O lines difficult. In the stacking process, the simulation cubes that constitute the individual redshift intervals were randomly shifted and rotated to avoid periodic replicas of the same large-scale structures. Then, after selecting a random observer within the cube at $z = 0$ we generate a single cone with a view of $5°\!.5 \times 5°\!.5$, and tag gas particles with their redshift, angular position, density, and temperature. Particles with temperatures in the range 10^5–10^7 K and overdensity $\delta < 1000$ are classified as the "WHIM phase." Among the remaining gas particles, those that provide a significant contribution to line emission are either in a "hot phase" ($\delta \geqslant 1000$ and $T \geqslant 10^7$ K, roughly corresponding to gas within clusters of galaxies) or in a "dense phase" ($\delta \geqslant 1000$, $T < 10^7$ K, typically associated with galaxy groups). Their contribution to the X-ray emission is included in our mock spectra. The contribution from particles colder than 10^5 K is negligible. In the mock spectra, we did not include the contribution from gas at $z > 0.51$. Emission lines (like the FeL complex in galaxy groups) from high-z gas potentially contaminates spectra in the energy range in which we search for WHIM lines. We estimate the impact of contamination by spurious lines in Section 6.1.

To account for the finite angular resolution of the instrument, the FOV of the light cone is divided into 256×256 pixels of $1'\!.3 \times 1'\!.3$, i.e., smaller than the planned CRIS resolution but possibly consistent with alternative instrument designs. The mock X-ray spectrum within each angular resolution element was obtained by adding together the individual spectra from each gas particle within the pixel plus that of gas particles in the contiguous pixels, weighted according to the smoothing kernel. The mock spectra were then sampled with an energy resolution of 1 eV to mimic the energy resolution of the instrument. The effect of the Galactic absorption has been included using the model of Morrison & McCammon (1983) in which we have adopted a typical high-latitude column density value of 1.8×10^{20} cm^{-2} (McCammon et al. 2002). We have assumed the same metal solar abundance as in the Anders & Grevesse (1989) models. The final result is a suite of $256 \times 256 \times 7$ mock spectra that we search for detectable WHIM lines. A typical example of mock spectrum is shown in Figure 1. The red curve represents the contribution by extragalactic gas in a light cone with FOV of $2'\!.6 \times 2'\!.6$ (i.e., the sum of $2 \times 2 \times 7$ individual mock spectra). Photon counts have been computed in $\Delta E = 1$ eV energy bins assuming a 1 Ms observation with CRIS. The spectrum is convolved with the detector response matrix of 1 eV energy resolution (FWHM). Emission lines from different metals are clearly visible. In particular, we have flagged those lines corresponding to a line system at $z = 0.033$. The O VII triplet and the O VIII recombination line are clearly visible. The black curve shows the sum of the contributions of the Galactic foreground and the unresolved extragalactic background modeled after McCammon et al. (2002). The Galactic O VII and O VIII lines at $z = 0$ are clearly seen in correspondence of their rest-frame energy.

3. ANALYSIS OF THE MOCK SPECTRA

To assess the possibility of detecting the WHIM in emission and constraining its thermal state with next-generation instrument, we consider spectra in larger pixels ($2'\!.6 \times 2'\!.6$) similar to

Figure 1. Emission spectrum in a 2.6×2.6 area taken in a 1 Ms observation with *Xenia* CRIS, assuming an energy resolution $\Delta E = 1$ eV. Black: sum of the Galactic foreground and unresolved extragalactic background. The Galactic O VII triplet and the O VIII Kα line at $z = 0$ are flagged. Red: contribution from the extragalactic gas. The O VII and O VIII lines at $z = 0.033$ are indicated in the plot.

(A color version of this figure is available in the online journal.)

the CRIS angular resolution (goal). For this purpose, we search for emission lines in each of the $128 \times 128 \times 7$ mock spectra using a two-step procedure. (1) We identify the O VII (triplet) and O VIII lines by searching for local maxima in the appropriate energy range of the spectrum. (2) We compute the SB of each line by summing the flux over energy bins redward and blueward of the line maximum and stop whenever the surface brightness SB_{th} in the bin drops below 7×10^{-3} photons s^{-1} cm^{-2} sr^{-1}, which is smaller than the typical line-detection threshold for a 1 Ms observation with CRIS, as we will show Section 3.2. A simple example serves to clarify the procedure. To identify O VIII lines produced in the redshift range $z = [0, 0.065]$ we search for local maxima in the energy range $[0.613, 0.653]$ eV, where the lower bound is the redshifted energy of an O VIII photon emitted at $z = 0.065$. The centroid of the line is identified with the maximum and its intensity is obtained by summing over all contiguous energy bins with SB above that of the selected threshold. This strategy, which minimizes the chance contamination from gas at different redshifts, cannot be applied to real spectra since we lack the information of the redshift of the gas responsible for the line emission. This effect is discussed in Section 6.1.

Detectable WHIM lines are rare and it is unlikely to find two of them in the same mock spectrum. On the other hand, when approaching the SB threshold, several weak emission lines start to appear. They are typically clustered around stronger lines and are thus likely to be physically associated to the same line-emitting element. Therefore, all these lines would spoil line statistics since they would oversample the same line-emitting regions. To circumvent this problem, we have adopted a simple criterion: we merge together all lines that are separated by a number of energy bins smaller than some minimum amount n_{bin}. In our analysis, we have adopted $n_{bin} = 8$ (corresponding to 8 eV) after having checked that the number of lines with 0.1 photons s^{-1} cm^{-2} sr^{-1} (strong enough to be hopefully detected by next-generation instruments) depends neither on n_{bin} nor on SB_{th}.

To confirm that our B2 model fulfills the current constraints on the soft X-ray diffuse background, we have compared the total SB predicted by the model in the [0.65, 1] keV band with that measured by Hickox & Markevitch (2007a) after removing the contribution from all known sources. According to the model, the WHIM contribution to the SB contributed is $(3.6 \pm 0.3) \times 10^{-13}$ erg cm^{-2} s^{-1} deg^{-1}, safely below the observed value of $(1.0 \pm 0.2) \times 10^{-12}$ erg cm^{-2} s^{-1} deg^{-1}. The more conservative B1 model, which predicts a lower SB is also obviously in agreement with observations.

3.1. Line Statistics

After having identified all O VII and O VIII emission lines in the mock spectra, we can compute their cumulative number per unit redshift as a function of the line SB. The top panel of Figure 2 shows the case of the O VII triplet whose SB is the sum of the three lines. The black continuous curves refer to model B2 while the red dashed curves refer to model B1. For each model, the upper curve accounts for the gas emission from all gas particles along the line of sight and the lower curve considers only the contribution from the "WHIM phase" (see Section 2.1). In the B2 model, the lines contributed by the warm-hot gas constitute a significant fraction of the total. However, this fraction decreases with the SB of the lines. It ranges from ∼100% for the weakest line to ∼5% for the brightest one. This result shows that the possibility of detecting the WHIM emission lines increases when decreasing the line-detection threshold and clearly illustrates the need for increasing the sensitivity of next-generation instruments. Model B1 predicts ∼30% less lines than model B2, as expected. The difference among the models is almost independent of the line SB. For a reference line SB of 0.1 photons s^{-1} cm^{-2} sr^{-1} (matching the typical detection threshold for next-generation X-ray spectrometers as we will show), the expected number of detected lines is of the order of unity, indicating that the chance of multiple line detections in a pixel is rather small.
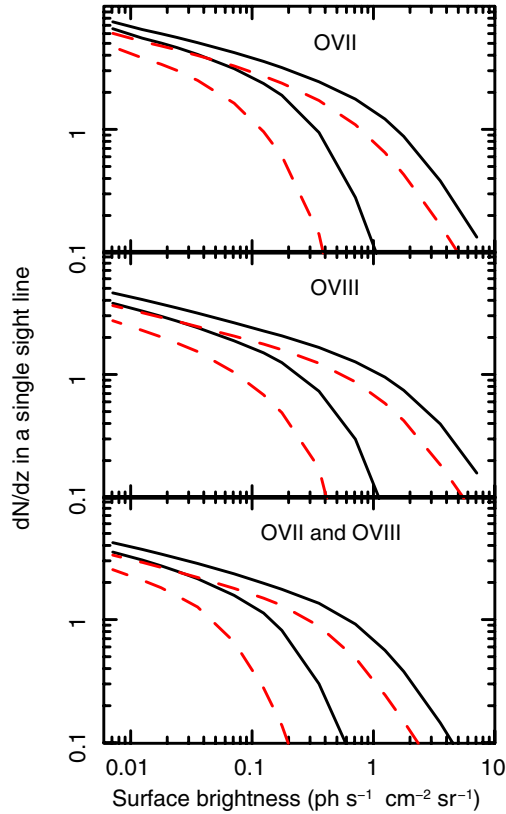
Figure 2. Cumulative number of emission lines per unit redshift as a function of line surface brightness. Each panel refers to O VII triplet (top), O VIII Lyα (middle), or both O VII triplet and O VIII Lyα (bottom). Black, solid curves indicate model B2, while red, dashed curves model B1. For each model, the upper curve shows all the gas and the lower curve refers to "WHIM phase" gas only.

(A color version of this figure is available in the online journal.)

The middle panel of Figure 2 shows the cumulative dN/dz statistics for the O VIII line. All considerations made for the O VII lines apply to the O VIII case except for the fact that for a given SB the expected number of O VII triplets is larger than that of O VIII lines. This difference becomes smaller if one considers the brightest O VII lines rather than the triplet. The bottom panel shows the cumulative dN/dz of those line systems that exhibit both the O VII triplet and O VIII line as a function of the total SB. The curves are similar to those of the O VIII lines (middle panel) except at the bright end. This is due to the fact that the presence of an O VIII line almost invariably guarantees that of an O VII triplet with similar (or larger) SB.

Our results can be compared with the theoretical predictions of Cen & Fang (2006) who used more sophisticated models that account for departures from ionization equilibrium and the effects of galactic superwinds. Their predicted cumulative number of emission lines (see Figure 12 of their paper) is similar to that predicted by model B2. In particular, the agreement is remarkable for the O VIII lines, while we seem to overpredict for O VII triplets. In addition, we note that the difference between model B1 and B2 is larger than the scatter in their model predictions, indicating that we are being generous in our attempt to bracket theoretical uncertainties.

3.2. Expected WHIM Detections

To detect O VII and O VIII emission lines, one needs to discriminate the genuine, weak emission signal from the astrophysical foreground and background, which represents the main source

of noise, typically exceeding the instrumental background. The problem of detecting the WHIM emission lines is analogous to that of detecting a low-SB source with a typical angular extension is a few arcmin, i.e., the typical angular size of a WHIM filament at $z \sim 0.3$, The signal to noise is then optimized by measuring spectra with an angular resolution comparable to that of the sources over large FOV to detect as many WHIM lines as possible. In practice, one wants to perform spatially resolved spectroscopy over large areas with an angular resolution of a few arcmin. The CRIS detector proposed for the *Xenia* mission, and which we are considering as a prototype for next-generation spectrographs, fulfills these requirements.

To investigate the possibility of detecting the WHIM through line emissions and assess the statistical significance of the detections, one needs to quantify the noise which is mainly contributed by two sources: the cosmic X-ray background (CXB, hereafter) produced by unresolved extragalactic point sources, and the foreground emission of our Galaxy.

The CXB is contributed by all X-ray sources (mostly AGNs) below the source detection threshold. Its intensity depends therefore on the characteristics of the detector and on the exposure time. A conservative upper limit to the CXB can be obtained from the X-ray Quantum Calorimeter rocket experiment (McCammon et al. 2002) since this estimate includes the contribution of all point sources in the FOV of ~ 1 sr. In this case, the CXB SB is $f_{CXB} \sim 30$ photons s^{-1} cm^{-2} sr^{-1} keV^{-1}. This value can be reduced by removing all resolved sources. One can remove sources previously detected in some other surveys. However, efficient removal would be possible only in areas covered by deep surveys, which are typically small. The alternative is to perform simultaneous deep imaging and resolved spectroscopy of the same areas, a strategy that would be possible if both a CCD-like imager and a two-dimensional spectrograph with similar FOVs were available. This is precisely the case of the *Xenia* mission concept which should be capable of resolving and removing ~ 1000 AGNs per square degree down to a limiting flux of 2.5×10^{-16} erg s^{-1} cm^{-2} in the 0.5–2 keV band. If AGNs were isotropically distributed, then a spectrograph with $\sim 4'$ angular resolution would have all its pixels contaminated by AGN emission. Taking into account the angular clustering of the AGNs (Vikhlinin & Forman 1995), this contamination would affect $\sim 63\%$ of the pixels if the angular resolution of the instrument is improved to 2.5 (i.e., the CRIS goal). It is clear that the best compromise between low AGN contamination and large number of available pixels depends on the actual characteristics of the detector and on the availability of a CCD imager. For the sake of simplicity in this work we adopt the conservative solution of keeping all pixels and thus we assume $f_{CXB} = 30$ photons s^{-1} cm^{-2} sr^{-1} keV^{-1}.

The Galactic foreground is basically contributed by three sources: the so-called Local Bubble, the Galactic halo, and the solar wind charge exchange (SWCX). Following McCammon et al. (2002), we describe the foreground emission as the sum of absorbed thermal model (*wabs* and *apec* model in the XSPEC package, respectively) and unabsorbed thermal model (*apec*). The former component represents the Galactic halo, while the latter the sum of the Local Bubble and SWCX. One may think that this model is too crude, since the SWCX contribution, which is non-thermal, is expected to outshine that of the Local Bubble. Moreover, the variable nature of the SWCX and the lack of strong observational constraints (e.g., Henley & Shelton 2008; Fujimoto et al. 2007) make it difficult to model its contribution. However, for the purpose of this work, this approximation is
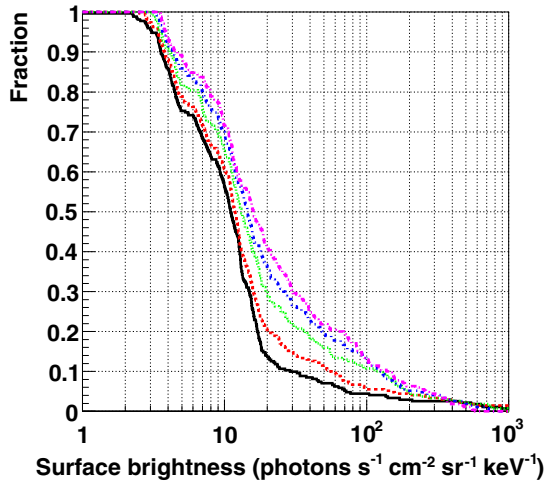
Figure 3. Fraction of energy bins (each bin with 1 eV width) in which the measured surface brightness is above the value indicated on the X-axis. Different curves represent different energy resolutions (FWHM) of the instrument: 1 eV (red dashed), 3 eV (green dotted), 5 eV (blue dot dashed), and 7 eV (magenta dash dotted). The black, solid curve shows the case of no convolution with the detector response.

(A color version of this figure is available in the online journal.)

reasonable for two reasons. First, it has been shown that the sum of two thermal components, although inaccurate, is quite effective in reproducing observations, at least within the energy resolution of CCD detectors (Galeazzi et al. 2007; Yoshino et al. 2009). Second, in the analysis of the real spectra one ignores the energy ranges in which Galactic emission lines are present. These lines include Lyβ, Lyγ, and Lyδ transitions from H-like C and N atoms, which should constitute strong features of the SWCX emission. In fact, all SWCX lines listed by Koutroumpa et al. (2006) and Bodewits et al. (2007) with a contribution of >a few% of O VII triplets are in energy intervals that we ignore when we search for the WHIM lines in Section 6.1.

Since the energy spectrum of the Galactic foreground is characterized by prominent emission lines (see Figure 1) and we are interested in identifying those produced by the WHIM, Galactic foreground flux cannot be estimated by the averaged flux over the wide energy range (e.g., 0.4–0.7 keV). More realistically, we would need to restrict the search to those energy bins that are not heavily contaminated by Galactic lines. Once again, when adopting this strategy one should compromise between the need for keeping as many energy resolution elements as possible and that of minimizing the Galactic signal. The solution can be found by looking at Figure 3 which shows the fraction of energy bins in which the measured foreground SB is above the value indicated on the X-axis. The shape of the curves that refer to the case of no convolution with the detector response (black, solid) and of 1 eV energy resolution (red, dashed) is characterized by a sharp drop at moderate SB values, followed by a flattening in the high-SB tail. This bi-modality reflects the transition from a regime in which the flux is dominated by the continuum contribution (the low-SB end) to a regime dominated by the emission of bright lines (the high-SB end). The transition occurs at an SB of $f_{FG} \sim 20$ photons s^{-1} cm^{-2} sr^{-1} keV^{-1}, which therefore we take as the reference value for the Galactic foreground continuum signal in this paper. The other curves of Figure 3 refer to different energy resolutions. As the energy resolution degrades, the fraction of high Galactic SB becomes larger. This influence is considered in Section 6.2.

Having estimated the two noise sources (f_{CXB} and f_{FG} to 30 and 20 photons s^{-1} cm^{-2} sr^{-1} keV^{-1}, respectively) and ignoring the negligible contribution from the instrumental noise (Kelley et al. 2007), one can compute the significance of a line detection from the following expression:

$$\sigma_{line} = \frac{f_{line}}{\sqrt{[f_{line} + (f_{CXB} + f_{FG})\Delta E]}} \sqrt{\Delta\Omega t_{exp} A_{eff}}, \qquad (1)$$

where f_{line} is the source line flux in units of photons s^{-1} cm^{-2} sr^{-1}, ΔE is the energy resolution of the instrument, A_{eff} its effective area, $\Delta\Omega$ its angular size (or the pixel size in case of this work), and t_{exp} is the exposure time. Equation (1) assumes that both signal and noise can be treated as Poisson variables.

In Table 1 we list for the two WHIM model explored (Column 1) and the two different exposure times considered in this work (Column 2), the minimum line SB required for a 5σ line detection calculated with Equation (1) in a hypothetical observation performed with CRIS (Column 3). The corresponding number of detections per resolution element and unit redshift can be obtained from the dN/dz statistics plotted in Figure 2. They are listed in Columns 4 (O VII), 5 (O VIII), and 6 (simultaneous O VII and O VIII detections). Column 7 shows the number of O VII+ O VIII WHIM detections expected in the 1 deg^2 FOV due to the gas at $z \leqslant 0.5$. Each entry in Columns 4–6 shows two values. The higher one represents the expected number of detected lines contributed by all gas, not just in the WHIM phase. The smaller one, in parenthesis, refers to lines that can be attributed to the WHIM. All detection estimates assume an angular resolution of $2\farcm6 \times 2\farcm6$ (corresponding to the sum of 2×2 pixels in the simulated data set to the CRIS goal resolution) and 1 eV energy resolution. These estimates do not account for the presence of spurious emission lines that contaminate $\sim 20\%$ of the energy band being analyzed. Their impact on the ideal detection estimates listed in Table 1 is estimated in Section 6.

From Table 1, we see that the expected number of detections is quite large even in the least favorable case (model B1, $t_{exp} = 100$ ks, simultaneous O VII + O VIII detection). However, only 1 Ms long observations guarantee the observation of WHIM lines in the most conservative scenario of model B1. With the more realistic model B2 one expects to be able to detect WHIM lines also with shorter (100 ks) exposure times. We note that WHIM detection estimates in Column 7 are to be regarded as conservative since they only consider gas out to $z = 0.5$ whereas hydrodynamical simulations show that the WHIM mass fraction is still quite large at $z = 1.0$. Overall, these results indicate that next-generation instruments will allow one to unambiguously detect the WHIM in emission and, as we will see in the next sections, to characterize its thermal state and trace its spatial distribution.

4. PHYSICAL PROPERTIES OF THE WHIM IN EMISSION

In this section, we investigate the physical properties (density ρ_{gas}, temperature T, and mass M) of the WHIM that, according to our results, can potentially be detected by deep resolved spectroscopy in next-generation X-ray missions. The relevant quantities obtained from the analysis of the mock X-ray spectra will be compared with the corresponding "true (input)" physical properties of the WHIM measured directly from the simulation. To perform realistic comparisons the "true" quantities were measured by averaging over all gas particles that contribute to the spectral signal, i.e., particles within volume elements. The data used for comparison are taken from the FOV of $5\fdg5 \times 5\fdg5$
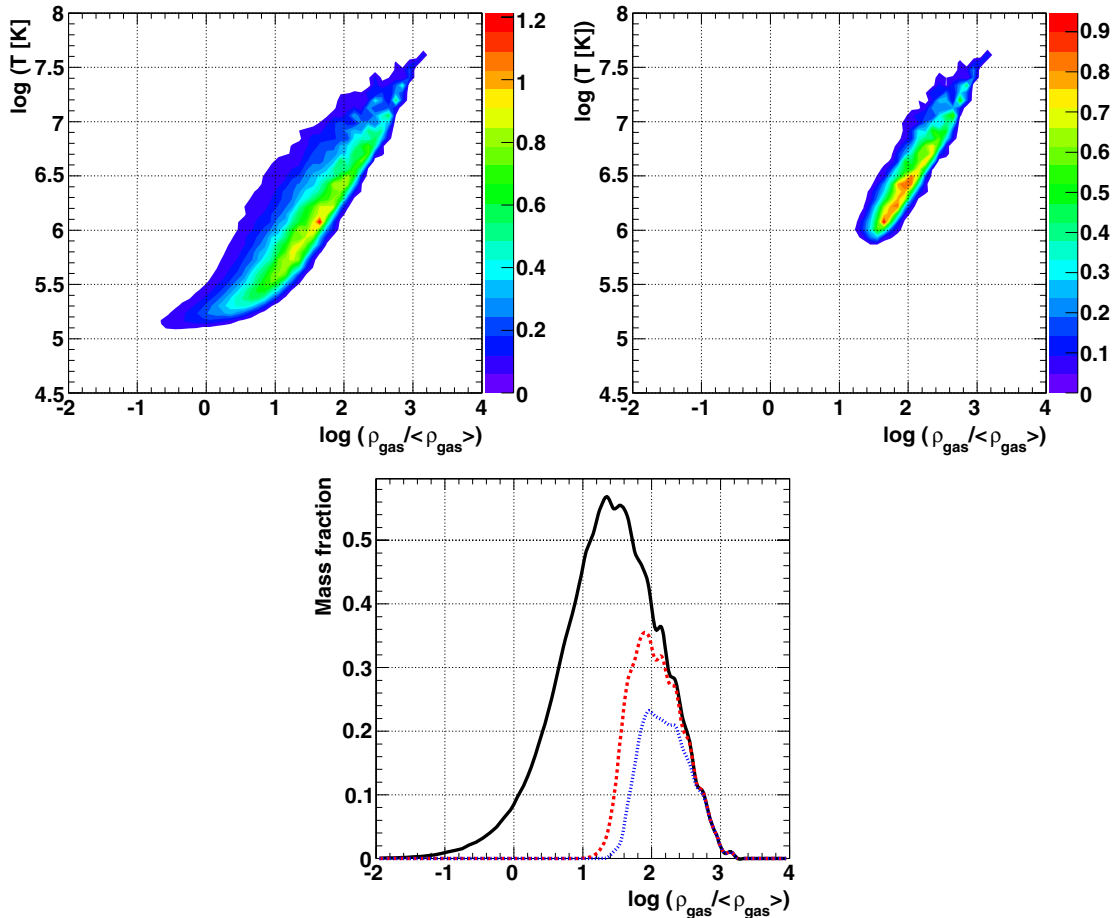
Figure 4. Top left: contours of constant gas mass fraction in phase-space, i.e., the fraction in unit $\log \rho$ and $\log T$ intervals. The gas density is normalized to its cosmic mean (X-axis) and its temperature is in units of K (Y-axis). The plots considers only gas particles in the redshift slice $0.202 < z < 0.274$ and with temperature $T > 10^5$ K. Color-coded contours are drawn with respect to different values of the gas mass fraction, indicated in the color scale. Top right: same as the top left panel, but referring to gas elements characterized by O VII + O VIII line systems strong enough to be detected with 1 Ms observation with CRIS. Bottom panel: the probability distribution function of the gas density obtained by merging the gas mass fraction in the ρ–T plane over its temperature. Black curve: all gas elements. Red dotted curve: gas elements in which both O VII and O VIII are above 5σ detection threshold of 0.07 photons s^{-1} cm^{-2} sr^{-1}, corresponding to 1 Ms exposure with CRIS. Blue dashed curve: same as the red dotted curve but referring to a 100 ks exposure with detection threshold of 0.48 photons s^{-1} cm^{-2} sr^{-1}.

Table 1
Emission Line Detections

Model	$t_{\rm exp}$	$f_{\rm line}$	$dN_{\rm O\,VII}/dz$	$dN_{\rm O\,VIII}/dz$	$dN_{\rm O\,VII+O\,VIII}/dz$	$N_{\rm O\,VII+O\,VIII}$ per deg^2
B2	1.0	0.07	4.2 (3.1)	2.6 (1.9)	2.4 (1.6)	639 (426)
B2	0.1	0.48	2.1 (0.6)	1.5 (0.5)	1.1 (0.2)	293 (53)
B1	1.0	0.07	3.3 (1.6)	2.1 (1.0)	1.8 (0.7)	479 (186)
B1	0.1	0.48	1.4 (0.03)	1.1 (0.05)	0.7 ($<10^{-3}$)	186 (0)

Notes. Column 1: WHIM model; Column 2: exposure time (Ms); Column 3: minimum line surface brightness required for a 5σ detection (photons s^{-1} cm^{-2} sr^{-1}); Column 4: expected number of O VII detections per resolution element and unit redshift; Column 5: expected number of O VIII detections per resolution element and unit redshift; Column 6: expected number of simultaneous O VIII and O VIII detections per resolution element and unit redshift; Column 7: expected number of simultaneous O VIII and O VIII detections per square degree due to gas within $z = 0.5$. All estimates assume an angular resolution of $2'.6 \times 2'.6$. The numbers in parenthesis indicate lines contributed by the WHIM.

and the redshift range of $0.202 < z < 0.274$. The angular size of each volume element is $2'.6 \times 2'.6$ (the angular resolution) in Section 4.1 and $1'.3 \times 1'.3$ in Section 4.2. The depth of a volume element is 3 Mpc (comparable to the energy resolution).

4.1. Density and Temperature of Detectable WHIM

The thermal state of the gas can be appreciated from the phase-space diagram shown in the top left panel of Figure 4. Color contours are drawn in correspondence of the same

gas mass fraction, indicated in the color scale. This plot is analogous to the one shown in Figure 6 of Branchini et al. (2009) with some important differences. First of all here we only consider particles with $T > 10^5$ K that are potentially relevant for the line emission. Second, this plot refers to redshift slice $0.202 < z < 0.274$, considerably narrower than $0 < z < 0.2$, the one considered by Branchini et al. (2009). Finally, and most important, the plot refers to gas density and temperature averaged in the $2'.6 \times 2'.6 \times 3$ Mpc volumes and
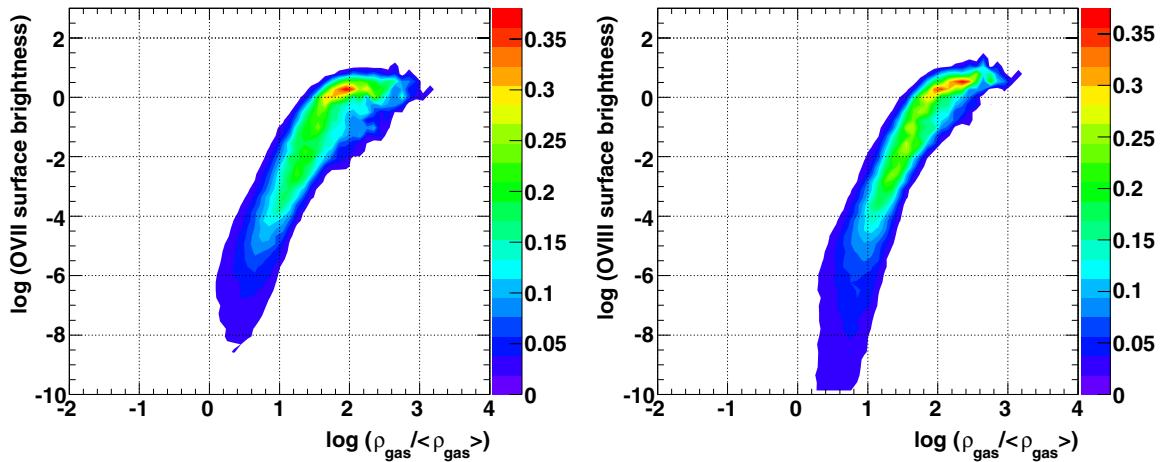
Figure 5. Contours of constant gas mass fraction in the line surface-brightnesses–gas-density plane. The plots consider only gas particles in the redshift slice $0.202 < z < 0.274$ and with temperature $T > 10^5$ K. The surface brightness (Y-axis) is in units of photons $\mathrm{s}^{-1}\,\mathrm{cm}^{-2}\,\mathrm{sr}^{-1}$ and the gas density (X-axis) is normalized to its cosmic mean. Left panel: surface brightness of the O VII triplet. Right panel: O VIII recombination line. The detection limit with a *Xenia* 1 Ms observation is 0.07 photons $\mathrm{s}^{-1}\,\mathrm{cm}^{-2}\,\mathrm{sr}^{-1}$, or $Y = -1.15$.

not to the density and temperature of each gas particle in the hydrodynamical simulation, which cannot be observed directly. The simulated data considered in Figure 4 refer to the full FOV of $5°.5 \times 5°.5$ but rather thin redshift slice to avoid large variation in the volume of the resolution elements. The smoothing effect induced by the volume averaging is very evident in the poor sampling of the high-density and high-temperature regions, when compared to Figure 6 of Branchini et al. (2009). The effect can be further appreciated by looking at the black curve in the bottom panel of Figure 4, which shows the probability distribution function of the gas density mass-weighted within each resolution element. The gas density on the X-axis is expressed in units of mean density. The distribution function, which was obtained by marking the phase-space plot over the gas temperature, looks remarkably symmetric. This symmetry is a result of the averaging process that deletes the high-density tail that characterizes the density distribution function of the gas particles (Davé et al. 2001).

The top right panel of Figure 4 is analogous to the top left one but considers only gas elements for which the combined O VII and O VIII line SB is above the 5σ detection threshold of 0.07 photons $\mathrm{s}^{-1}\,\mathrm{cm}^{-2}\,\mathrm{sr}^{-1}$, line systems that could be detected with 1 Ms observation with CRIS. This plot clearly indicates that next-generation instruments will preferentially probe the hottest part of the WHIM with $T > 10^6$ K with typical density $\delta_g \sim 100$, hence confirming the results of Bertone et al. (2010).

This result is better illustrated by the red dotted curve in the bottom panel of Figure 4 which is analogous to the black curve but only refer to the gas that can be potentially detected in a 1 Ms observation. It clearly shows that detectable emission lines preferentially probe high-density regions. The integral of the red dotted curve shows that 30% of the total gas mass (the integral of the black curve) could be probed via emission line spectroscopy. The remaining 70% of the gas that will go undetected typically resides in regions with density below 40 times the cosmic mean and constitutes the bulk of the WHIM. Reducing the exposure time to 100 ks further decreases the fraction of detectable gas to $\sim$20% and shifts its mean density to larger values (blue dashed).

To further investigate the issue of the WHIM detectability, we plot in Figure 5 the contours of gas mass fraction as a function of gas density (X-axis) and line SB (Y-axis). The two plots refer to the O VII triplet (left panel) and O VIII line (right panel),

respectively, and consider all gas elements with $T > 10^5$ K as in the top right panel of Figure 4. The first thing to notice is the very large range (about 10 order of magnitudes) of line SB. Deep observations with a *Xenia* like mission will be capable of probing the gas above a detection limit of $\sim$0.1 photons $\mathrm{s}^{-1}\,\mathrm{cm}^{-2}\,\mathrm{sr}^{-1}$. The expected line SB spans $\sim$2 order of magnitude when $\delta_g \gtrsim 100$. Below this value, and for a line SB below the detection threshold, the isoprobability contours run almost parallel to the Y-axis, indicating the difficulty of detecting gas in lower density environment: huge improvements in instrumental sensitivity would be required to probe the bulk of the WHIM in emission.

4.2. Estimating the Gas Temperature

The quantitative analysis of the mock spectra allows us to investigate the thermal properties of the emitting gas, namely, to estimate the gas temperature. For those spectra in which both the O VII and O VIII lines have been detected, one can use the line ratio to estimate the gas temperature. Alternatively one could estimate the gas temperature by comparing the relative intensity of the resonance, forbidden, and intercombination lines of the O VII triplet. These, however, can be detected only in $\sim$20% of the cases. Therefore, in this section we assess how well one can measure the gas temperature from the O VII–O VIII line intensity ratio when the CIE hypothesis holds true. For this purpose, we have compared the temperature estimated from the mock spectra to the "true" temperatures of the gas responsible for line emission. The latter quantity, however, is not uniquely defined for two reasons. First, there is no one-to-one correlation between the measured quantity, which is derived from the line intensity, and the temperature of the gas particles. Second, the line-emitting regions are sampled in finite volume elements because of the angular/energy resolution of the spectrometer. To tackle this problem, we will use different estimators of the "true" temperature and compare the results with the temperature estimated from the O VII–O VIII line intensity ratio.

In Figure 6, we have plotted the correlation between the temperature measured from the mock spectra (X-axis) and the one obtained from three different gas temperature estimators (Y-axis). Here we consider the case of model B2 only. In the plot the different colors indicate the three different estimators: O VII-line-emission-weighted temperature (black crosses)
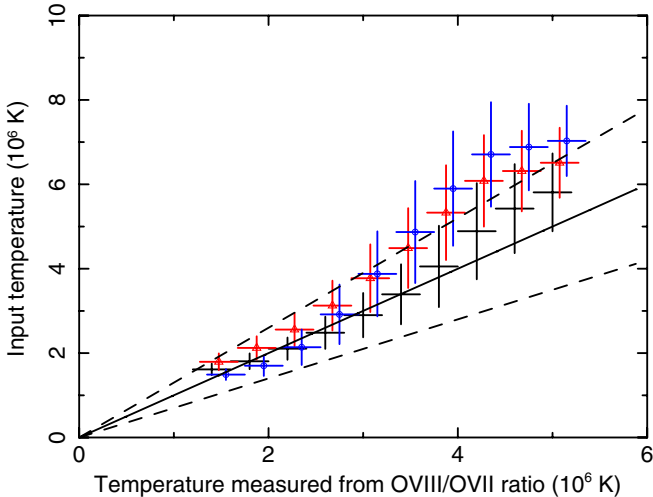
Figure 6. Relation between the gas temperature measured from the O VIII–O VII line intensity ratio in the mock WHIM spectra (*X*-axis) and different estimators for the underlying temperature of the gas (*Y*-axis). The *Y*-axis of the black crosses, red triangles, and blue circles refer to O VII-emission-weighted temperature, O VIII-emission-weighted temperature, and density-weighted temperature, respectively. The data are taken from the FOV of $5°.5 \times 5°.5$ and the redshift range of $0.202 < z < 0.274$. The angular size of each volume element is $1'.3 \times 1'.3$. Horizontal error bars correspond to the temperature bin size, while the vertical bars represent the scatter among resolution elements in the temperature bin. The perfect correlation (i.e., $Y = X$) is represented by the central solid line. The two external dashed lines represent $Y = 1.3X$ and $Y = X/1.3$, respectively.

(A color version of this figure is available in the online journal.)

O VIII-line-emission-weighted temperature (red triangles) mass–density-weighted temperature (blue circles). The "true" gas temperature is estimated in those resolution elements where the SB of both O VII and O VIII is above 0.07 photons s^{-1} cm^{-2} sr^{-1}. The vertical size of each cross represents the scatter about the mean. The horizontal bar represents the size of the corresponding temperature bin.

The plot shows that a tight correlation between the measured and the "true" temperature is found with all the estimators used. The temperature estimated from the O VIII–O VII line intensity ratio seems to best trace the O VII-emission-weighted temperature of the gas, which is expected since temperature estimated from spectral lines preferentially weight those regions in which line emission is stronger. When the O VIII-emission-weighted temperature is used the correlation is still tight but the slope is larger than unity. This is due to the fact that this estimator preferentially weights regions in which the O VIII is strong, i.e., regions in which the temperature is typically higher than those from which the O VII photons come from. With the mass–density-weighted temperature the relation is unbiased for temperatures below $T \sim 3 \times 10^6$ K and then the correlation becomes steeper. This behavior can be understood as follows. The temperature measured from the spectra is sensitive to $T = (2–3) \times 10^6$ K, where O VII and O VIII emissivity has a peak and it is reliably traced by the mass-weighted temperature. At higher temperatures, a large fraction of the gas is too hot to contribute to the O VII emission and therefore it is not traced by the O VII line. As a result, the measured temperature underestimates the mass-weighted temperature of the gas.

Our assumption of CIE is well justified for gas in high-density and -temperature environments ($\delta_g \gtrsim 100$ and $T \gtrsim 2 \times 10^6$ K). Photoionization becomes non-negligible in regions characterized by lower density and temperature (i.e., when $\delta_g \lesssim 100$ and $T \lesssim 2 \times 10^6$ K). The presence of the photoionizing background would change the ionization state of the gas. In particular, this background would ionize O VII into O VIII (Chen et al. 2003), thus enhancing the intensity of the O VIII emission line relative to that of O VII. As a consequence, assuming the O VII/O VIII ratio of CIE overestimates the temperature of the gas. However, these effects will affect the gas properties in regions of moderate overdensity and temperature which could hardly be observed through emission line spectroscopy with current and next-generation detectors.

These results show that one can use the measured O VII and O VIII lines to estimate the temperature of the gas with reasonable precision (10%–20% uncertainty, depending on the gas temperature). The measured quantity probes the temperature of the gas responsible for O VII emission and underestimates that of the O VIII emitting regions. The measured quantity also traces the temperature of the bulk of the gas for $T = (1–3) \times 10^6$ K and underestimates it in hotter regions.

Finally, we note that we have assumed a detector with angular resolution $1'.3 \times 1'.3$ and that we do not consider the line broadening due to the detector response. The rationale behind this choice of the angular resolution is to reduce possible systematics in the estimate of the "true" temperature. In fact, using an angular resolution of $2'.6 \times 2'.6$, as in the rest of the paper, would not appreciably change the value of the measured temperature but would artificially reduce the estimated "true" temperature of the gas because of the increase in the filtering volume associated with the resolution element. A good angular resolution is thus important for an accurate determination of the physical state of the WHIM. Including the effect of the line broadening induced by the energy resolution of the detector would reduce the number of detectable line systems and would increase the statistical errors. However, we do not expect that these errors will seriously affect our temperature estimates since temperature errors are driven by the presence of multi-phase gas within the resolution elements and not by the limited line statistics.

5. PROBING THE SPATIAL DISTRIBUTION OF THE WHIM

Spatially resolved spectroscopy provides the unique possibility of tracing the spatial distribution of the WHIM. In this section, we use our simulated two-dimensional spectra to investigate the three-dimensional distribution of the WHIM responsible for detectable line emission. Here we focus our attention on the WHIM model B2 and assume a 1 Ms observation with a CRIS-like spectrometer with angular resolution of $2'.6 \times 2'.6$, energy resolution of 1 eV and effective collecting area of 1000 cm^2.
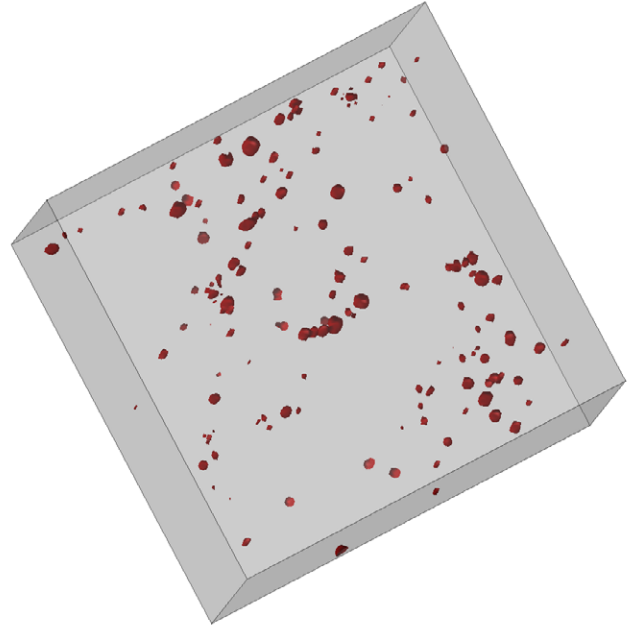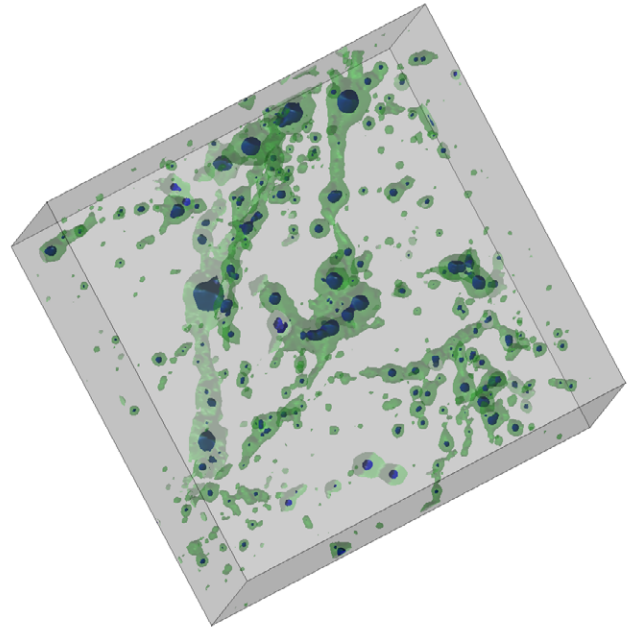
We only consider systems in which both O VII and O VIII lines can be detected at $\geqslant 5\sigma$ significance and ignore the possibility of using additional metal lines associated with the source. The need for using both lines is dictated by the need for measuring the redshift of the associated line-emitting region. This is guaranteed by selecting line pairs with energy ratio consistent with that of the O VII and O VIII lines. Using additional metal lines can, in principle, improve the identification of line-emission systems and the determination of their redshift. However, the benefit in using these extra lines is in practice limited by the associated increase in chance contaminations. For example, a number of emission lines from the FeL complex can be seen in the mock spectra. However, these lines typically probe the hotter part of the WHIM, typically associated with virialized structure also responsible for strong continuum emission which reduces the significance of line detections. The Ne IX is a better
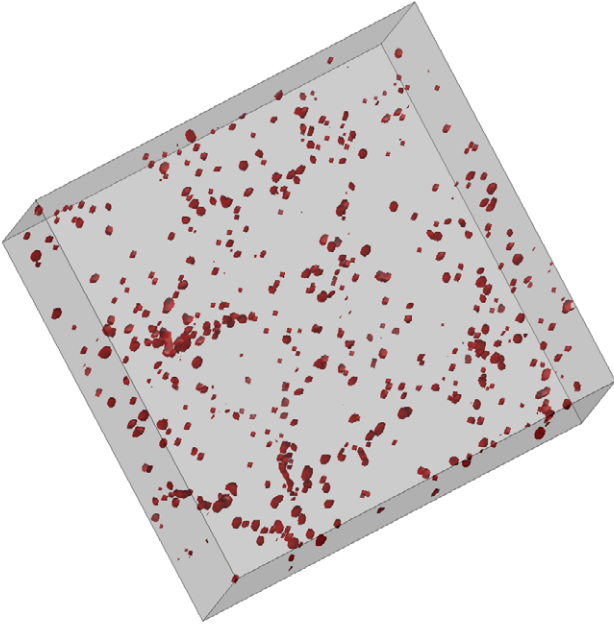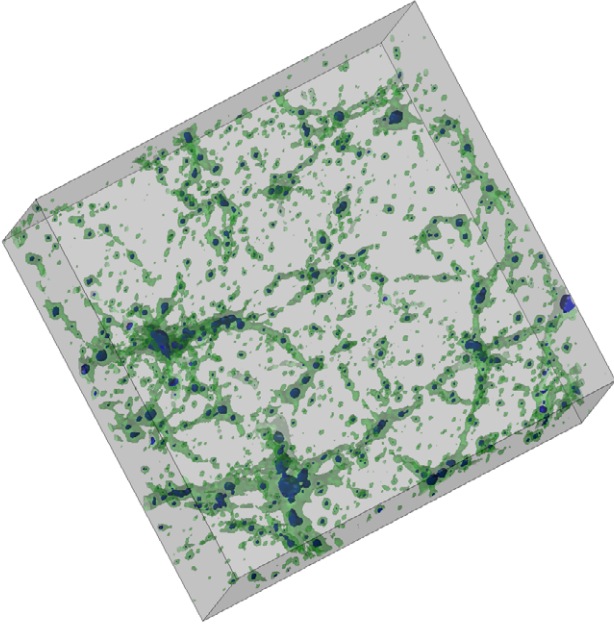
Figure 7. Slice of gas density contour (top) and O emission map (bottom) at $z = 0.2117$–0.2317, corresponding to comoving distance of 603–657 h^{-1} Mpc. The field of view is $5°.5 \times 5°.5$. The blue region of the top panel corresponds to $\rho_{gas}/\langle\rho_{gas}\rangle = 75$, while the green region corresponds to $\rho_{gas}/\langle\rho_{gas}\rangle = 10$. The red regions (blobs) show where both O VII and O VIII lines are identified with $>5\sigma$ significance, with 1 Ms exposure by *Xenia* CRIS-like instrument.

Figure 8. Same as Figure 7, but slice at $z = 0.0805$–0.1004, corresponding to comoving distance of 237–294 h^{-1} Mpc. The field of view is $5°.5 \times 5°.5$.

signpost for the WHIM since it probes gas with $T \sim 10^{6.6}$ K. However, its emission line is too close to the Fe L lines to eliminate the risk of spurious detection. Finally, the energies of the redshifted N and C lines are typically found at the edges of the instrumental range, where a forest of emission lines due to L and M transition of heavier metals exists. For all these reasons, we search the spectra for emission systems characterized by the O VII Kα resonance and O VIII Lyα pair and do not look for additional ion lines.

Figures 7 and 8 compare the three-dimensional distribution of the selected O VII + O VIII line systems (lower panels) with the

spatial distribution of the gas in the simulation (upper panels). Both figures show the same FOV of $5°.5 \times 5°.5$, corresponding to a 6×6 mosaic with CRIS, but refer to two different redshift slice. Figure 7 refers to the redshift interval $z = [0.2117, 0.2317]$ corresponding to a 54 h^{-1} Mpc slice at a comoving distance of 630 h^{-1} Mpc in the cosmological model of the hydrodynamical simulation. Figure 8 shows a much closer slice of 57 h^{-1} Mpc at a comoving distance of 265 h^{-1} Mpc, corresponding to $z = [0.0805, 0.1004]$.

In the gas map, the blue regions correspond to isodensity surfaces drawn at $\rho_{gas}/\langle\rho_{gas}\rangle = 75$. The green surfaces correspond to regions characterized by smaller overdensity $\rho_{gas}/\langle\rho_{gas}\rangle = 10$. At these overdensity levels the spatial distribution of the gas in the simulation is characterized by the well-known network of filaments punctuated by virialized structures

that, in this isocontour maps, appear as quasi-spherical "blobs." The filamentary structure is more clearly seen in the more distant slice thanks to the large volume sampled. The gas distribution in the nearby slice is clearly more dominated by a few, prominent structures, as expected.

The red regions in the bottom panels identify the positions of the selected O VII + O VIII line systems. Clearly, these line systems qualitatively trace, in a sparse fashion, the large-scale structures of the gas with overdensity $\rho_{gas}/\langle\rho_{gas}\rangle = 75$. However, the tracing is not unbiased since the line systems tend to undersample the more massive virial structures associated with the largest blob. This bias reflects the unfavorable ion balance for O VII and O VIII within hot virialized regions. The fact that O VII + O VIII line systems are poor tracers of gas at lower overdensity ($\rho_{gas}/\langle\rho_{gas}\rangle = 10$) confirms the fact that emission lines preferentially sample the fraction of the WHIM that resides in high-density regions (Figure 4).

This qualitative analysis confirms that next-generation X-ray spectrometers could be successfully used to trace the spatial distribution of the WHIM through its line emission. Thanks to the large number of the detected emission line systems, more quantitative analysis can be performed through statistical estimators. In Ursino et al. (2011), which uses the same mock spectra, it is shown that the two-point spatial correlation function of the line emitters could be measured with good accuracy. Its slope and correlation length, which should be similar to those of the galaxies, could be estimated at a few percent accuracy level.

The tracing of underlying gas by the detected line systems, which in the plots looks quite patchy, is possibly improved by adopting some adaptive smoothing technique like those based on the Wavelet transform analysis. The improvement would be particularly noticeable for nearby structures since, in this cases, the angular size of the associated gas cloud is larger than the angular resolution of the instrument.

6. ROBUSTNESS TESTS AGAINST NON-IDEAL EFFECTS

In this section, we assess the impact of foreground emission, energy resolution, and contamination from spurious metal lines on the detectability of the extragalactic O VII and O VIII lines and on our capability of tracing the spatial distribution of the WHIM.

6.1. Impact of Contamination from Spurious Lines and High Continuum

We address the problem of identifying O VII and O VIII lines with no a priori knowledge of the nature of the detected lines and of their redshift. For this purpose, the line-detection procedure has been modified from that depicted in Section 3.2. The rationale behind this choice is to avoid contamination from lines associated with different line-emitting regions along the line of sight and to account for the fact that the line-detection efficiency is not constant across the FOV since the level of the continuum emission depends on the direction. We have decided to ignore additional metal lines associated with the WHIM since their search would increase the chance of false identifications. To identify the putative WHIM emission systems, we do not perform spectral fitting assuming some particular model but we search for the O VII Kα and O VIII Lyα line pairs with a strategy more conservative than that adopted in Section 3 and designed to account for the variable spectral continuum and for the presence of spurious spectral features. The procedure is as follows. (1) We deal with the fact that the continuum

level may vary along the spectrum and also from spectra to spectra, across the FOV. To account for this effect, we modify the line-detection criterion: instead of setting a fixed line-detection threshold, corresponding to a minimum line SB, we define the detection significance S by comparing the number of photon counts in 1 eV bin (Counts) with the number of continuum counts (Continuum) obtained by averaging over the neighboring 50 eV that do not contain line features above 2σ or known galactic lines brighter than >0.05 photons s^{-1} cm^{-2} sr^{-1} eV^{-1}. The significance is then defined as

$$S/N = \frac{\text{Counts} - \text{Continuum}}{1.0 + \sqrt{\text{Continuum} + 0.75}}, \qquad (2)$$

where the denominator is an approximate 1σ Poisson error (Gehrels 1986). Note that Equation (2) is a similar quantity as Equation (1) but is calculated with observed quantities. (2) We consider only lines in the energy range [375, 653] eV detected at 5σ significance (i.e., signal-to-noise ratio (S/N) > 5). With this criterion, we identify 7.8×10^3 lines deg^{-2} corresponding to transitions of highly ionized ions of N, O, Ne, and Fe. (3) We minimize the chance of contamination by spurious lines by enforcing a number of constraints: (a) we reject all lines with flux of >0.05 photons s^{-1} cm^{-2} sr^{-1} eV^{-1} that could be attributed to Galaxy emission, i.e., all known Galactic lines; (b) to avoid oversampling the same structures we discard all lines with energy within 15 eV from that of a stronger emission line; and (c) we search for line pairs from the same angular element, and pick up the pairs only if the energy interval of the two lines is the same as that of redshifted O VII Kα resonance and O VIII Lyα lines. The emission lines without an associated O VII or O VIII line are discarded.

Using the procedure, we only consider those systems in which both the O VII Kα and the O VIII Lyα lines are identified with significance larger than 5σ. As a result, 446 deg^{-2} line-emission systems are identified. This number is ∼30% less than those identified in Section 3. The discrepancy comes from the combined effect of line contamination and high continuum level. We confirm that, with this procedure, the contamination of chance coincidence of either O VII or O VIII lines with heavier metal lines is less than 10%. Our spectra do not include photons emitted by gas at $z > 0.5$. O VII lines emitted beyond this redshift would be redshifted out of the energy range probed by the detector, so the only impact of high-redshift gas would be to increase the probability of contamination by higher energy lines such as O VIII, Ne IX, Ne X, and Fe L complex. However, we do not expect a severe additional contamination for two reasons. First, the dimming of the emission line intensity, which scales as $(1 + z)^{-3}$, is not exactly counterbalanced by the increase in the probed volume since the latter decreases more slowly than $\propto (1 + z)^3$ at high redshifts Second, at higher redshifts the mass fraction of the gas in the Lyα forest increases while the abundance of the gas contributing to O, Ne, and Fe lines emission decreases. To test the validity of these hypotheses and quantify line contamination by high-redshift gas, we have created and analyzed mock spectra that accounts for emission by the gas out to $z < 1.2$ and within an FOV of 2°.6 × 2°.6 and have compared the results with the reference case of $z < 0.5$. Including the emission from gas beyond $z = 0.5$ decreases the number of detectable O VII–O VIII pairs by only 10%–15%.

6.2. Impact of Energy Resolution

A degradation in the energy resolution of the instruments affects the possibility of detecting the WHIM lines in two ways.
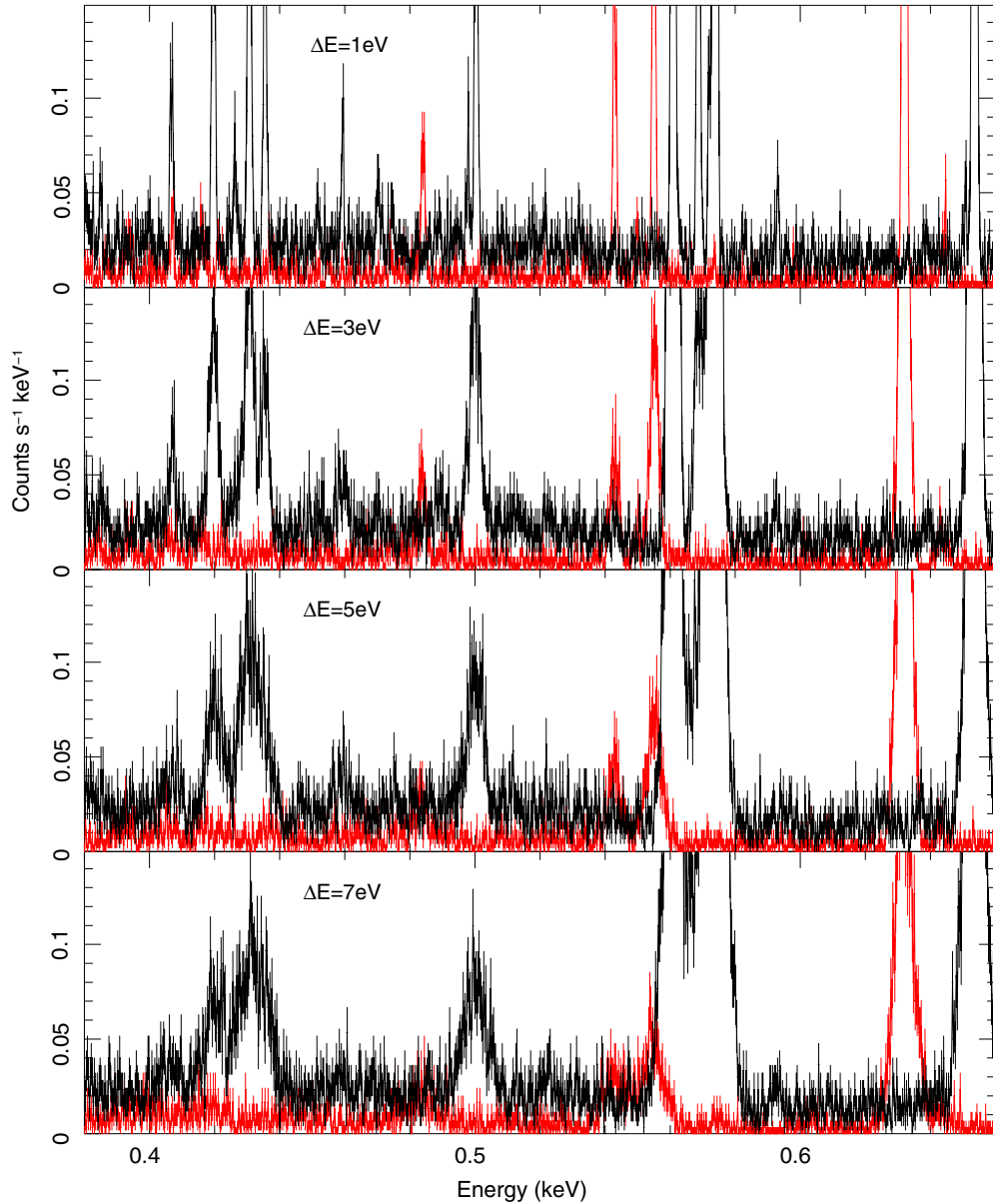
Figure 9. Mock spectrum in a $2'.6 \times 2'.6$ area from a 1 Ms exposure with *Xenia* CRIS. The black spectra are the sum of Galactic foreground and unresolved extragalactic background emission, while the red is extragalactic diffuse gas. The four panels of the each plot show the spectra convolved with the energy resolution (FWHM) of 1 eV, 3 eV, 5 eV, and 7 eV, respectively.

First, it decreases the S/N in Equation (1). As a consequence, one needs to increase the SB threshold for 5σ detections, hence reducing the total number of detected lines. Second, with a large ΔE the chance of contamination from neighboring lines increases. Here we let the energy resolution vary in the range [1,7] eV which encompasses the values already achieved with the current instrument ($\Delta E = 7$ eV with *Suzaku*; Kelley et al. 2007) and the energy resolutions expected by currently planned X-ray missions equipped with a microcalorimeter spectrograph.

A visual impression of the cumulative impact of these two effects is given by Figure 9, which shows a portion of the mock emission spectrum displayed in Figure 1 but observed with different energy resolutions and on a log scale. With 1 eV resolution (FWHM), O VII triplets and O VIII resonant line at $z = 0.033$ (0.55 keV and 0.63 keV, respectively) are clearly detected, with a marginal detection of a emission line at 0.47 keV. With $\Delta E = 3$ eV, the 0.47 keV line is below detection threshold, and with $\Delta E = 5$ eV the O VII triplet becomes hard

to observe because of the local ($z = 0$) O VII emission. When ΔE is 7 eV, the O VII triplet drops below the detection threshold.

A quantitative assessment of the contamination by spurious lines is provided by Figure 3. The fraction of energy bins with SB above that of the Galactic foreground emission ($f_{\mathrm{FG}} = 20$ photons s^{-1} cm^{-2} sr^{-1} keV^{-1}) steadily increases with ΔE: from 20% for $\Delta E = 1$ eV to 41% for $\Delta E = 7$ eV. In Table 2 we quantify how energy resolution affects the number of expected detections, splitting its effect into two: the increase of the SB detection threshold (Column 3) and the increase in the number of bins contaminated by the Galactic foreground (Column 4). All estimates assume the same setup as in Table 1 apart from the energy resolution: WHIM model B2, 1 Ms observation, and $2'.6 \times 2'.6$ angular resolution. The first effect is rather minor and reduced the expected number of line detection only by <20%. On the other hand, contamination by galactic foreground has a more serious impact since the number of expected detection is directly proportional to that of the uncontaminated energy bins.

Table 2
Number of Emission Line Detections with Different Detector Energy Resolution

ΔE (eV)	f_{line} (photons s^{-1} cm^{-2} sr^{-1})	$dN_{\rm O\,VII+O\,VIII}/dz$ $\cdots$	Fraction of High f_{FG} (%)	$N_{\rm O\,VII+O\,VIII}$ per deg^2 in the Simulation
$\cdots$ [a]	0.07	2.4	14	446
1	0.07	2.4	20	396
3	0.11	2.1	30	351
5	0.13	2.0	36	274
7	0.15	1.9	41	163

Notes. Column 1: detector energy resolution; Column 2: minimum line SB required for a 5σ detection (photons s^{-1} cm^{-2} sr^{-1}); Column 3: expected number of simultaneous O VIII and O VIII detections per resolution element and unit redshift. The foreground emission is assumed to have a constant SB of 20 photons s^{-1} cm^{-2} sr^{-1} keV^{-1}; Column 4: fraction of the energy range where foreground emission SB exceeds 20 photons s^{-1} cm^{-2} sr^{-1} keV^{-1}; Column 5: number of simultaneous O VIII and O VIII detections per square degree in the mock spectra. All estimates assume an angular resolution of $2'.6 \times 2'.6$ and model B2.
[a] Not convolved with detector energy resolution. The bin size is 1 eV.

Our results show that decreasing ΔE from 1 to 7 eV reduces the number of expected detection by a factor of two. It should also be noticed that this effect does not randomly affect all emission line systems. The systems that are more seriously affected are those with redshifted emission lines that coincide with those of the Galactic foreground. This induces a non-trivial selection effect in the redshift distribution of the WHIM emitters that need to be corrected for to trace their three-dimensional distribution.

To quantify the impact of the energy resolution on the expected number of WHIM line detections, we have repeated the analysis performed in Section 6.1 after convolving the mock spectra with the appropriate response matrix. In the analysis of the response-convolved spectra, we again do not fit the spectra with a particular model, but searched for the O VII and O VIII line pairs. The only difference is that in the new analysis photon counts in neighboring energy bins are summed up before searching for emission lines. This is done to collect photons that are spread into several energy bins (the bin width is 1 eV) due to the energy resolution of the instrument. The results of this procedure obviously depend on the number of neighboring bins to be summed upon. We set this free parameter by maximizing the number of detectable emission lines. It turns out that the best results are obtained when summing over $((\Delta E/1\,{\rm eV}) + 1)$ bins for $\Delta E \leqslant 5\,{\rm eV}$ and over $((\Delta E/1\,{\rm eV}) - 3)$ for $\Delta E = 7\,{\rm eV}$. The change of the trend for $\Delta E = 7\,{\rm eV}$ reflects the fact that at low energy resolution foreground contamination becomes the limiting factor. The number of expected detections is listed in Column 5 of Table 2. It is clear that an energy resolution $\Delta E \leqslant 3\,{\rm eV}$ is desirable, although even with $\Delta E = 7\,{\rm eV}$ one still expects 160 O VII + O VIII line detections per square degree. The reason why the number of expected detection of the "no convolution" case is different from the analogous one listed in Table 1 is because in the line-detection strategy used in this case, and described in Section 6.1, we have ignored the energy range in which the SB of the foreground emission is above f_{FG}. These ranges could be also be searched for detectable lines by locally increasing the detection threshold. However, the expected increase in the number of detections is small since the intensity of the foreground emission lines is typically an order of magnitude larger than that of the WHIM lines.

7. DISCRIMINATING AMONG WHIM MODELS

As discussed in Section 2, current limitations in our understanding of the stellar feedback, chemical evolution, and metal
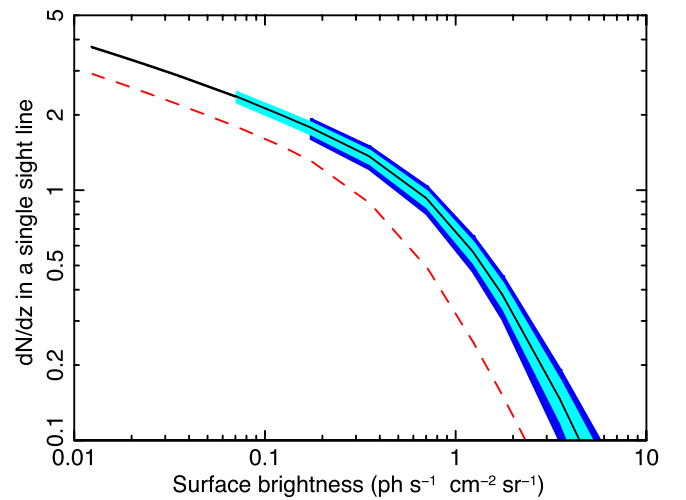
Figure 10. Expected dN/dz curve with a Poisson error with 1 Ms exposure, $2'.6 \times 2'.6$ angular size, and 1 deg^2 FOV with CRIS. The black curve is the model curve (model B2). Color-filled areas are 1σ Poisson error regions: cyan and blue are without considering detector energy resolution and with convolution with 7 eV energy resolution, respectively. Red dashed line is from model B1 (Poisson error is not shown).
(A color version of this figure is available in the online journal.)

diffusion process are reflected in the large uncertainties of the WHIM models. The most recent hydrodynamical simulations of the intergalactic gas at low redshifts have been used to construct different WHIM models by assuming different, physically plausible, recipes for the above processes. Comparisons between model predictions and observations can therefore constrain the cosmic history of chemical evolution and metal diffusion along with the underlying stellar feedback processes by discriminating among these WHIM models. UV observations are leading the way, since they currently provide the most stringent constraints on the WHIM models through O VI line statistics. X-ray observations can add additional constraints, through line statistics, direct assessment on the physical state and spatial distribution of the emitting gas.

In this section, we assess to what extent future experiments will enable us to discriminate among different WHIM models. Here we focus on the dN/dz statistics of O VII and O VIII lines. Figure 10 shows the expected number of O VII + O VIII detections per unit redshift in an angular resolution element of $2'.6 \times 2'.6$ and for 1 Ms observation with CRIS for model B2 (black, continuous curve) and B1 (red, dashed). The

cyan-colored band around the black lines shows the 1σ Poisson uncertainties for model B2 from the finite number of detections expected in a 1 deg^2 FOV. The expected errors are much smaller than the difference between model B1 and B2, suggesting that observations will efficiently discriminate among different WHIM models. The capability of constraining the physical processes that regulate the WHIM is further illustrated by pointing out that the difference between model B1 and model B2 is of the same order as that between the WHIM models proposed by Cen & Fang (2006), which adopt different prescription for the ionization balance and for galactic superwinds. The larger, blue uncertainty strips that extend beyond the SB threshold of 0.15 photons s^{-1} cm^{-2} sr^{-1} refer to the case of $\Delta E = 7$ eV. It shows that even with a rather modest energy resolution the discriminatory power of the dN/dz test is still considerably large. The significance of discriminating between the two models is 3σ–5σ with a 1 deg^2 observation, depending on the energy resolution.

It should be noted that the cosmic variance introduces an additional error in determining the dN/dz curve. We have estimated the contribution of cosmic variance by splitting the simulated $5^\circ\!.5 \times 5^\circ\!.5$ field into several smaller regions. The variance in detectable emission line systems is 20%, 15%, and 10%, for FOV of 0.25 deg^2, 1.0 deg^2, and 4.0 deg^2, respectively. Hence, a large-field mapping with >4.0 deg^2 is desirable to make the uncertainty due to cosmic variance smaller than the statistical error ($\sim$10% for 7 eV energy resolution). This can be easily achieved with dedicated missions such as *EDGE* and *Xenia*, thanks to the large FOV.

Finally, we point out that emission-line studies provide better statistics than absorption studies because of the comparatively larger number of line detections. In fact, the two approaches are very complementary. Emission studies preferentially probe regions of enhanced density where the impact of stellar feedback is larger and chemical enrichment is presumably stronger. On the contrary, absorption studies preferentially probe regions of moderate overdensity where the bulk of the WHIM resides and thus are indicated to be best for closing the baryon budget at $z = 0$. Space missions like *EDGE*, *Xenia*, and *ORIGIN* are designed to perform both emission and absorption analyses thanks to their capability of fast re-pointing that will enable us to use gamma-ray bursts as a distant beacon and search for the characteristic absorption features of the intervening WHIM (Branchini et al. 2009).

Constraining abundance and physical properties of the WHIM from observations is not straightforward. The first reason is that in order to trace the thermal history of the WHIM it requires an accurate and self-consistent treatment of the metal line cooling which, instead, is ignored in the present work. The second reason is the approximate treatment of a number of processes and quantities (galactic winds, AGN feedback, stellar IMF, and sub-resolution turbulence; see Bertone et al. 2010; Oppenheimer & Davé 2009; Smith et al. 2011; Schaye et al. 2010), which may affect the thermal state of the WHIM in the current numerical experiments. Some of these processes have little impact on observable quantities such as O VIII SB (e.g., Bertone et al. 2010), and hence cannot be used to discriminate among competing WHIM models. On the other hand, emission line statistics and analysis will no doubt help to lift some of the model degeneracy, especially when coupled to observational constraints on the spatial distribution of the line-emitting gas, like those derived from the estimate of the angular and spatial two-point correlation function of the O-line emission (Ursino et al. 2011).

8. DISCUSSION AND CONCLUSIONS

In this work, we have analyzed the mock X-ray spectra extracted from the hydrodynamical simulation of Borgani et al. (2004) to investigate the possibility of detecting the WHIM in emission with next-generation X-ray satellites, assess its thermal state, and trace its spatial distribution. Our theoretical predictions are based on the WHIM model of Branchini et al. (2009). The theoretical predictions presented in this work are mainly based on their model "B2", although we do consider the more conservative (and less realistic) WHIM model "B1" to bracket theoretical uncertainties. Finally, the experimental setup considered here is the same one proposed for the *Xenia* mission. In particular, we will assume that our mock spectra were "observed" with the imaging spectrometer CRIS.

We showed that a CRIS-like spectrograph will enable us to detect a large number of O VII + O VIII line-emitting systems, to estimate their temperature from the line ratio, and to trace their spatial distribution. The line systems are expected to trace the hotter and denser part of the WHIM, typically associated with the outskirts of large virialized structures. Our results suggest that the number of expected detections is large enough to discriminate among different WHIM models and to constrain the physical processes that regulate its thermal state and metal content, even when one accounts for contamination effects and allows for a moderate ($\sim$7 eV) energy resolution.

All the results presented in this work are based on a WHIM model that fulfills all observational constraints but is nevertheless poorly constrained by observations. From the theoretical side, WHIM models suffer from the limited knowledge of the feedback mechanisms and metal diffusion processes that potentially affect the WHIM properties. In particular, the WHIM model adopted here, though effective in describing observations, lacks self-consistency since the metallicity of the gas is assigned in the *post-processing* phase rather than being computed during the run. To fix these problems, one should modify theoretical prescriptions for the feedback process or metal diffusion and gas cooling. Let us assess qualitatively the impact of having ignored line cooling. Efficient metal cooling requires a cooling time $t_{\rm cool}$ shorter than the Hubble time $t_{\rm H}$. With no metal cooling, $t_{\rm cool} < t_{\rm H}$ only when $\delta_g > 1000$. Cooling becomes more efficient in the presence of metals and less efficient with gas temperature, i.e., $t_{\rm cool}$ decreases with metallicity (e.g., Figure 4 of Wiersma et al. 2009), and increases with T. On the other hand, we have shown that emission line spectroscopy can only detect gas with $T > 10^6$ K (Figure 4). Taking all this into account and assuming a reference metallicity of $\sim$0.1$Z_\odot$ one finds that $t_{\rm cool} < t_{\rm H}$ if $\delta_g > 300$ for $T = 10^6$ K and if $\delta_g > 1000$ for $T = 2 \times 10^6$ K. These simple arguments indicate that metal line cooling preferentially affects dense ($\delta_g > 300$) gas typically associated with galaxy groups rather than the WHIM. Indeed, inefficient cooling in the simulation is probably the cause of the excess X-ray emission from groups in the simulation.

In fact, the impact of the metal cooling is likely to be more significant because it affects the whole thermal history of the baryons (Wiersma et al. 2009; Oppenheimer & Davé 2009; Smith et al. 2011; Tepper-García et al. 2011). When metals are transferred from galaxies, either by galactic wind or AGNs, both the density and metallicity are high, and hence metal cooling is very efficient. After the temperature is lowered by metal cooling, the gas is further cooled down by adiabatic expansion. As a result, the thermal state of baryons at $z \sim 0$ is determined by their thermal history. The impact of these effects can only be assessed by running a numerical simulation in which metal

cooling is accounted for self-consistently and, more importantly, in which the relevant physical process is included correctly. However, current numerical experiments which include a self-consistent treatment of metal cooling (Bertone et al. 2010) seem to corroborate our qualitative argument since they show that metal cooling mostly affects regions with overdensity typical of galaxy groups, rather than the WHIM. For this reason, we are quite confident that considering predictions from both model B2 and the very conservative model B1 will allow us to bracket theoretical uncertainties, including incorrect treatment of metal cooling in the numerical simulation.

Bertone et al. (2010) have shown that predictions of the detectability of the O VIII line are quite robust to the different model prescription with the exception of the cooling function. They show that using a metal-dependent cooling instead of a metal-independent scheme (as in our model) decreases the SB of the O VIII line in regions populated by *non*-WHIM by up to an order of magnitude, but does not significantly alter the line-emission properties in regions of lower overdensity where the WHIM typically resides. Reducing the artificially large brightness of large-density regions would decrease the noise level and increase the probability of detecting the emission line systems associated with the WHIM.

From these considerations, we conclude that our WHIM models are adequate for assessing the detectability through O VII/O VIII line pairs of the WHIM in emission and are confident that theoretical uncertainties are effectively bracketed, perhaps too generously, in the scatter among B1 and B2 model predictions. On the other hand, the gas distribution in the phase-space (Figure 4) and in the three-dimensional space (Figures 7 and 8), especially in regions of high density and moderate temperature, might not be accurate because of the approximate treatment of gas cooling in the simulations.

The results presented in this paper assume CIE. This is a reasonable hypothesis since a large part of O VII and O VIII lines that next-generation instruments are expected to detect are likely to be produced by warm-hot gas in high-density environments where the CIE is a fairly good assumption ($\delta_g \gtrsim 100$ and $T \gtrsim 2 \times 10^6$ K). The validity of the CIE hypothesis can be directly checked by analyzing a number of spectral features. One is the relative comparison of the intensity of the resonant, forbidden, and intercombination lines of the O VII triplet, which also provide an estimate of the gas temperature, alternative to that obtained from the O VIII/O VII ratio (see, e.g., Porquet et al. 2001). The possibility of performing this test, however, is limited to the few cases in which the components of the triplets can be unambiguously detected. From the analysis of the mock spectra, only in 30% of the cases we can detect both the resonant and the forbidden lines. The weaker intercombination lines is only detected for ~10%. If photoionization plays a role, O VIII line is also emitted from lower temperature gas, in addition to O VII triplets. Therefore, the number of detected line systems would increase because lower density ($\delta \lesssim 200$) regions also become detectable. The ionization state of the gas in this low-density regions would be affected and the temperature would be overestimated under the assumption of CIE.

Our analysis of the spatial distribution of the line-emission systems presented in Section 5 is rather qualitative. A more quantitative analysis, based on the mock spectra described in this work, is presented in Ursino et al. (2011), in which it is shown that the number density of detectable emission line systems is large enough to characterize the distribution by means of the spatial two-point correlation function. It is also shown that the two-point correlation function of the WHIM is significantly different from that of the *non*-WHIM and similar to that of galaxies with which the line-emitting WHIM is associated. Its correlation properties do not seem to evolve significantly in the redshift range $z = [0, 0.5]$, and the dynamical state, induced from the velocity-driven anisotropies in the observed clustering, is consistent with that of a gas coherently falling toward larger structures.

The main results of this work are summarized as follows. While the analyses are based on the specifications of CRIS on board *EDGE* or *Xenia*, essentially the same conclusions are applicable for *DIOS* or *ORIGIN*, which are equipped with a spectrometer of slightly different FOV, angular resolution, and effective area.

1. The WHIM can be detected in emission through O VII and O VIII lines. Unambiguous detection of the line systems requires the simultaneous detection of both lines, each one with statistical significance above 5σ. With a 1 Ms observation and in an FOV of 1 deg^2 we expect to detect ~640 O VII + O VIII line-emitting systems. A significant number of detections (~300 deg^{-2}) is still expected with a much shorter (100 ks) observation. These results are in broad agreement with those of Cen & Fang (2006).

2. A significant number of these line systems, however, trace gas that is hotter or denser than the WHIM ($\delta > 1000$). The number of line systems contributed by the WHIM is ~65% (i.e., ~430 deg^{-2}) for a 1 Ms observation. The fraction drops to ~20% when the exposure time is reduced to 100 ks. In other words, deep observations are required to detect a number of line systems large enough to investigate the statistical properties of the WHIM. Shorter observations would preferentially probe hotter gas in high-density environments associated with clusters or groups.

3. The expected large number of detections is robust. If one considers the very conservative model B1, which we have implemented to assess theoretical uncertainties, the number of line systems above 5σ detection threshold is still large (~480 deg^{-2}), 40% of which is contributed by the WHIM. The difference between model B2 and model B1 provides generous estimate of the theoretical uncertainties, larger than the scatter among the model predictions of Cen & Fang (2006).

4. The number of detectable systems is affected by contamination from spurious lines and by the level of the continuum that may vary with energy and direction. It is confirmed that a more rigorous detection procedure that accounts for both effects misses only ~30% of the line systems that are originally selected.

5. The number of detectable emission lines decreases with the energy resolution. However, even with an energy resolution of 7 eV, already achieved by the microcalorimeter on board *Suzaku*, one expects to detect ~160 O VII + O VIII line systems per deg^2 in a 1 Ms observation.

6. Detectable line systems preferentially trace the denser regions of the WHIM with typical gas overdensity of $\delta_g \sim 100$, typically associated with virialized structures like galaxies, groups, and the outskirts of galaxy clusters. Increasing the instrumental sensitivity will not significantly change these results since the bulk of the WHIM that resides in lower density environment is characterized by a very low line emissivity. These results agree with those of Bertone et al. (2010) and illustrate the importance of studying the

WHIM both in emission (to assess its spatial distribution and thermal state) and in absorption (to probe low-density regions and close the baryon budget).

7. In the region where CIE holds, the temperature of the gas associated with the detectable emission systems can be reliably estimated from the O VII/O VIII line ratio in the range of $(1–5) \times 10^6$ K, with typical random errors of $\sim 20\%$. The measured temperature traces the O VII-emission-weighted temperature of the gas, which, for $T = (1–3) \times 10^6$ K, probes the bulk of the gas in the emitting region.

8. With 400–600 line-emission systems detected per square degree, one can trace the spatial distribution of the line-emitting gas, a large fraction of which is in the warm-hot phase. The visual inspection of the emission maps confirms that the selected line systems trace the large-scale filamentary structure of the gas with typical overdensity $\rho_{gas}/\langle\rho_{gas}\rangle \geqslant 75$. Since line emission is associated with the denser part of the WHIM, the tracing is rather sparse and concentrated around the virialized structures that punctuate the filaments. Moreover, because of the unfavorable ionization balance, the tracing is biased against the largest virialized structures such as galaxy clusters that are typically found at the nodes of the network of filaments.

9. The observed dN/dz relation can be compared to theoretical predictions to discriminate among WHIM models and constrain the physical processes that regulate its thermal state and chemical composition. As an example we have shown that the dN/dz statistics is capable of discriminating among different metallicity models with a significance of 3σ–5σ with a 1 deg^2 observation, depending on the energy resolution. Further constraints will be provided by the analysis of the three-dimensional distribution of the line-emission systems and by combining these results with those obtained from the analysis of the absorption spectra.

REFERENCES

Anders, E., & Grevesse, N. 1989, Geochim. Cosmochim. Acta, 53, 197
Barlow, T. A., & Tytler, D. 1998, AJ, 115, 1725
Bertone, S., Schaye, J., Dalla Vecchia, C., Booth, C. M., Theuns, T., & Wiersma, R. P. C. 2010, MNRAS, 407, 544
Bodewits, D., et al. 2007, A&A, 469, 1183
Borgani, S., et al. 2004, MNRAS, 348, 1078
Branchini, E., et al. 2009, ApJ, 697, 328
Bregman, J. N. 2007, ARA&A, 45, 221
Buote, D. A., Zappacosta, L., Fang, T., Humphrey, P. J., Gastaldello, F., & Tagliaferri, G. 2009, ApJ, 695, 1351
Burles, S., & Tytler, D. 1997, AJ, 114, 1330

Burrows, D. N., Hartmann, D., Kouveliotou, C., Piro, L., den Herder, J., & Ohashi, T. 2010, Proc. SPIE, 7732, 77321T
Cen, R., & Fang, T. 2006, ApJ, 650, 573
Cen, R., & Ostriker, J. P. 1999a, ApJ, 519, L109
Cen, R., & Ostriker, J. P. 1999b, ApJ, 514, 1
Cen, R., & Ostriker, J. P. 2006, ApJ, 650, 560
Chen, X., Weinberg, D. H., Katz, N., & Davé, R. 2003, ApJ, 594, 42
Croft, R. A. C., Di Matteo, T., Davé, R., Hernquist, L., Katz, N., Fardal, M. A., & Weinberg, D. H. 2001, ApJ, 557, 67
Danforth, C. W. 2009, in AIP Conf. Proc. 1135, Future Directions in Ultraviolet Spectroscopy, ed. M. E. van Steenberg, G. Sonneborn, H. W. Moos, & W. P. Blair (Melville, NY: AIP), 8
Danforth, C. W., & Shull, J. M. 2005, ApJ, 624, 555
Danforth, C. W., & Shull, J. M. 2008, ApJ, 679, 194
Danforth, C. W., Stocke, J. T., & Shull, J. M. 2010, ApJ, 710, 613
Davé, R., et al. 2001, ApJ, 552, 473
den Herder, J. W., et al. 2011, Exp. Astron., in press (arXiv:1104.2048)
Fang, T., Buote, D. A., Humphrey, P. J., Canizares, C. R., Zappacosta, L., Maiolino, R., Tagliaferri, G., & Gastaldello, F. 2010, ApJ, 714, 1715
Fang, T., Davis, D. S., Lee, J. C., Marshall, H. L., Bryan, G. L., & Canizares, C. R. 2002, ApJ, 565, 86
Fujimoto, R., et al. 2004, PASJ, 56, L29
Fujimoto, R., et al. 2007, PASJ, 59, 133
Fukugita, M., Hogan, C. J., & Peebles, P. J. E. 1998, ApJ, 503, 518
Fukugita, M., & Peebles, P. J. E. 2004, ApJ, 616, 643
Galeazzi, M., Gupta, A., Covey, K., & Ursino, E. 2007, ApJ, 658, 1081
Galeazzi, M., Gupta, A., & Ursino, E. 2009, ApJ, 695, 1127
Gehrels, N. 1986, ApJ, 303, 336
Gupta, A., Galeazzi, M., Koutroumpa, D., Smith, R. K., & Lallement, R. 2009, ApJ, 707, 644
Haardt, F., & Madau, P. 1996, ApJ, 461, 20
Henley, D. B., & Shelton, R. L. 2008, ApJ, 676, 335
Henley, D. B., Shelton, R. L., & Kuntz, K. D. 2007, ApJ, 661, 304
Hickox, R. C., & Markevitch, M. 2007a, ApJ, 671, 1523
Hickox, R. C., & Markevitch, M. 2007b, ApJ, 661, L117
Kaastra, J. S., Werner, N., Herder, J. W. A. D., Paerels, F. B. S., de Plaa, J., Rasmussen, A. P., & de Vries, C. P. 2006, ApJ, 652, 189
Kawahara, H., Yoshikawa, K., Sasaki, S., Suto, Y., Kawai, N., Mitsuda, K., Ohashi, T., & Yamasaki, N. Y. 2006, PASJ, 58, 657
Kelley, R. L., et al. 2007, PASJ, 59, 77
Klypin, A., Hoffman, Y., Kravtsov, A. V., & Gottlöber, S. 2003, ApJ, 596, 19
Komatsu, E., et al. 2009, ApJS, 180, 330
Koutroumpa, D., Lallement, R., Kharchenko, V., Dalgarno, A., Pepino, R., Izmodenov, V., & Quémerais, E. 2006, A&A, 460, 289
Kravtsov, A. V., Klypin, A., & Hoffman, Y. 2002, ApJ, 571, 563
Mannucci, F., Bonnoli, G., Zappacosta, L., Maiolino, R., & Pedani, M. 2007, A&A, 468, 807
Mathur, S., Weinberg, D. H., & Chen, X. 2003, ApJ, 582, 82
McCammon, D., et al. 2002, ApJ, 576, 188
Morrison, R., & McCammon, D. 1983, ApJ, 270, 119
Narayanan, A., Savage, B. D., & Wakker, B. P. 2010a, ApJ, 712, 1443
Narayanan, A., Wakker, B. P., Savage, B. D., Keeney, B. A., Shull, J. M., Stocke, J. T., & Sembach, K. R. 2010b, ApJ, 721, 960
Nicastro, F., et al. 2005, Nature, 433, 495
Ohashi, T., et al. 2010, Proc. SPIE, 7732, 77321S
Oppenheimer, B. D., & Davé, R. 2008, MNRAS, 387, 577
Oppenheimer, B. D., & Davé, R. 2009, MNRAS, 395, 1875
Paerels, F., Kaastra, J., Ohashi, T., Richter, P., Bykov, A., & Nevalainen, J. 2008, Space Sci. Rev., 134, 405
Piro, L., et al. 2009, Exp. Astron., 23, 67
Porquet, D., Mewe, R., Dubau, J., Raassen, A. J. J., & Kaastra, J. S. 2001, A&A, 376, 1113
Rasmussen, A. P., Kahn, S. M., Paerels, F., Herder, J. W. D., Kaastra, J., & de Vries, C. 2007, ApJ, 656, 129
Rauch, M. 1998, ARA&A, 36, 267
Roncarelli, M., Moscardini, L., Tozzi, P., Borgani, S., Cheng, L. M., Diaferio, A., Dolag, K., & Murante, G. 2006, MNRAS, 368, 74
Schaye, J., et al. 2010, MNRAS, 402, 1536
Shen, S., Wadsley, J., & Stinson, G. 2010, MNRAS, 407, 1581
Smith, B. D., Hallman, E. J., Shull, J. M., & O'Shea, B. W. 2011, ApJ, 731, 6
Smith, R. K., Brickhouse, N. S., Liedahl, D. A., & Raymond, J. C. 2001, ApJ, 556, L91
Smith, R. K., Edgar, R. J., Plucinsky, P. P., Wargelin, B. J., Freeman, P. E., & Biller, B. A. 2005, ApJ, 623, 225
Smith, R. K., et al. 2007, PASJ, 59, S141
Spergel, D. N., et al. 2003, ApJS, 148, 175

Springel, V. 2005, MNRAS, 364, 1105
Springel, V., & Hernquist, L. 2003, MNRAS, 339, 289
Takei, Y., Henry, J. P., Finoguenov, A., Mitsuda, K., Tamura, T., Fujimoto, R., & Briel, U. G. 2007, ApJ, 655, 831
Tepper-García, T., Richter, P., Schaye, J., Booth, C. M., Dalla Vecchia, C., Theuns, T., & Wiersma, R. P. C. 2011, MNRAS, 413, 190
Tornatore, L., Borgani, S., Viel, M., & Springel, V. 2010, MNRAS, 402, 1911
Tripp, T. M., Bowen, D. V., Sembach, K. R., Jenkins, E. B., Savage, B. D., & Richter, P. 2006, in ASP Conf. Ser. 348, Astrophysics in the Far Ultraviolet: Five Years of Discovery with FUSE, ed. G. Sonneborn, H. W. Moos, & B.-G. Andersson (San Francisco, CA: ASP), 341
Tripp, T. M., Sembach, K. R., Bowen, D. V., Savage, B. D., Jenkins, E. B., Lehner, N., & Richter, P. 2008, ApJS, 177, 39
Ursino, E., Branchini, E., Galeazzi, M., Marulli, F., Moscardini, L., Piro, L., Roncarelli, M., & Takei, Y. 2011, MNRAS, in press (arXiv:1009.5519)
Ursino, E., & Galeazzi, M. 2006, ApJ, 652, 1085
Ursino, E., Galeazzi, M., & Roncarelli, M. 2010, ApJ, 721, 46

Viel, M., Branchini, E., Cen, R., Matarrese, S., Mazzotta, P., & Ostriker, J. P. 2003, MNRAS, 341, 792
Viel, M., Branchini, E., Cen, R., Ostriker, J. P., Matarrese, S., Mazzotta, P., & Tully, B. 2005, MNRAS, 360, 1110
Vikhlinin, A., & Forman, W. 1995, ApJ, 455, L109
Weinberg, D. H., Miralda-Escude, J., Hernquist, L., & Katz, N. 1997, ApJ, 490, 564
Werner, N., Finoguenov, A., Kaastra, J. S., Simionescu, A., Dietrich, J. P., Vink, J., & Böhringer, H. 2008, A&A, 482, L29
Wiersma, R. P. C., Schaye, J., & Smith, B. D. 2009, MNRAS, 393, 99
Yoshikawa, K., Yamasaki, N. Y., Suto, Y., Ohashi, T., Mitsuda, K., Tawara, Y., & Furuzawa, A. 2003, PASJ, 55, 879
Yoshikawa, K., et al. 2004, PASJ, 56, 939
Yoshino, T., et al. 2009, PASJ, 61, 805
Zappacosta, L., Maiolino, R., Mannucci, F., Gilli, R., & Schuecker, P. 2005, MNRAS, 357, 929
Zappacosta, L., Nicastro, F., Maiolino, R., Tagliaferri, G., Buote, D. A., Fang, T., Humphrey, P. J., & Gastaldello, F. 2010, ApJ, 717, 74